



Monitoring Induced Seismicity in the Montney, Northeast British Columbia

Geoscience BC Report 2021-18

A.M.M. Bustin

Jones, D., Chalmers, G., Amini, A., Bustin, R.M.



Summary

A better understanding of the processes controlling the occurrence and magnitude of anomalous seismicity induced by hydraulic fracturing of the Montney Formation in Northeast British Columbia is needed to develop more effective protocols for mitigation and prevention. The limited availability of monitoring data to researchers is arguably the greatest challenge to the advancement of our understanding of anomalous seismicity induced by hydraulic fracturing operations. In this study, we have designed, built, and tested a telemetered array of 15 stations with accelerographs paired with geophones to densely monitor for induced seismicity. Our array design provides a low-cost alternative to broadband and force-balance accelerometer arrays for monitoring fluid injection and storage activities, even in areas with low magnitude (ex. 0.5) traffic-light protocols. Additionally, our array provides data for researchers not available through broadband arrays or single force-balance accelerometers. We demonstrate that a dense array of accelerographs is required to map the asymmetrical attenuation resulting from rupture directivity effects observed for $M > 1.5$ events and is therefore required to understand the hazard from induced seismicity, such as whether an event will be felt or cause damage. We further demonstrate that our array of surface geophones is capable of obtaining event solutions for small- to micro-seismicity, which may be crucial for the proactive mitigation of induced seismicity and to provide input data and comparative results for modelling studies.

Early models conceptualized fluid-injection induced seismicity as resulting from seismic slip on faults directly induced by the diffusion of increased pore pressures (IOGCC, 2015); however, the largest events recorded in the Montney Trend in Northeast British Columbia (the Montney) from hydraulic fracturing completions in the Montney Formation do not follow the pattern predicted by the pore pressure diffusion model. We demonstrate how 3D hydro-geomechanical modelling can be used to better understand the processes and parameters controlling anomalous induced seismicity. Through comparing models with different residual friction values for the fault, we suggest the mechanisms responsible for the observed variations in anomalous seismicity induced by hydraulic fracturing. A model with slip-weakening represents cases with seismicity observed to follow patterns typical of a pore pressure diffusion model, with events increasing in magnitude with injection time. In comparison, the slip-strengthening case predicts fewer, lower magnitude events with the maximum magnitude event occurring earlier in time. The most hazardous events are predicted by a model with slip strengthening near the fluid injection and slip-weakening on the outer fault. Such a model predicts the highest magnitude events, early in time, without precursor events with $M>2$. We suggest this mechanism is responsible for the $M>4$ events induced by hydraulic fracturing observed in the Montney.

Introduction

One of the greatest challenges for assessing and mitigating the hazard and risk from anomalous induced seismicity (AIS) in the Montney Trend in Northeast British Columbia is the limited monitoring data available to researchers. The need for increased monitoring and data sharing was referred to directly or indirectly in many of the recommendations regarding induced seismicity from the Scientific Review of Hydraulic Fracturing in British Columbia (Scientific Hydraulic Fracturing Review Panel, 2019). While the regional broadband network and local operator-deployed broadband array in the Montney is sufficient for larger events ($M>1$), a more complete catalogue of events is required for detailed modelling studies and proactive mitigation, which was the first objective of this project. At the time this project was initially proposed to Geoscience BC (2015), microseismic surveys were still regularly conducted; however, the number of microseismic surveys decreased once the project was funded and underway (2017). The coverage of accelerometers in NEBC also remains inadequate to understand whether events will be felt or cause damage. To address this data gap, with the support of Geoscience BC, we have developed a telemetered array of paired accelerograph plus geophone stations to densely monitor hydraulic fracturing operations.

Our original array consisted solely of accelerographs; however, we recognized during the deployment of our first-generation stations in 2017 that our digital noise levels were too high to accurately detect operationally-induced events. As much of the proposed objectives require information on operationally-induced events (i.e. expected microseismicity, $\sim M<1$) and we did not have access to surveys where microseismic was being recorded, we expanded our sensor design to include geophones in order to collect this data. Detailed monitoring of operationally-induced events provides data to map the fracture and fault geometry and data for history matching numerical modelling studies necessary to understand conceptual models, test mitigation measures, and develop forecasting frameworks. Real-time monitoring of operationally-induced events may also enable proactive mitigation, as fault activations can be identified (summarized in Scientific Hydraulic Fracturing Review Panel, 2019). Therefore, we also added collecting real-time solutions from the geophone data into our project.

We have thoroughly tested our three-component (3C) accelerographs and our sensors have fulfilled the regulatory requirements of the BC Oil and Gas Commission (BCOGC) for the ground motion monitoring of 8 hydraulic fracturing operations in the Montney. Additionally, 9 of our paired stations were installed to monitor a small hydraulic fracturing operation in the Montney in the fall of 2020. During the dense deployment, there were two additional hydraulic fracturing operations within the monitoring area, one overlapping in time with the main operation we were monitoring and the other

following the second operation. A fourth hydraulic fracturing operation was also completed at the same time, 26 km southeast from the pad we were monitoring.

A second objective of this project was to integrate data recorded by our array(s) into 3D probabilistic hydro-geomechanical models to investigate the impact of mitigation strategies and improve our understanding of the processes and parameters controlling anomalous induced events. Early models conceptualized fluid-injection induced seismicity as resulting from seismic slip on faults directly induced by the diffusion of increased pore pressures from fluid injection (IOGCC, 2015); however, the largest events recorded in the Montney do not follow the pattern predicted by the pore pressure diffusion model. The largest events occurred early in time, without precursor events with M>2 (Scientific Hydraulic Fracturing Review Panel, 2019) and thus could not have been mitigated by traffic light protocols. A better understanding of the processes controlling the magnitude and frequency of anomalous events induced by hydraulic fracturing operations therefore is needed before better mitigation and prevention frameworks can be developed. In an attempt to understand why the two largest events induced by hydraulic fracturing in the Montney did not follow the anticipated pore pressure diffusion model, while many other operations do, we here test a different conceptual model where fluid injection induces aseismic slip on a fault, which then triggers seismic slip (Bhattacharya and Viesca, 2020; Eyre et al., 2019; Guglielmi et al., 2020; Wynants-Morel et al., 2020). We test this conceptual model by comparing the resulting slip on a fault from fluid injection through hydraulic fractures for different values of fault residual friction and compare the results to the variations in fault behaviours we observed during our monitoring operations.

This report begins with a presentation of our station design and is followed by a summary and our interpretations of our accelerometer data. The geophone data, a detailed description of our processing, and our interpretations from the dense paired-station deployment are then presented. Finally, our 3D hydro-geomechanical modelling is presented and the results are discussed.

Station Design

The design for our low cost, mobile, easy to install stations was modified from the early earthquake detectors developed by the Earthquake Engineering Research Facility (EERF) at UBC and installed in British Columbia schools for the Earthquake Early Warning System (<http://globalnews.ca/news/2429129/early-warning-system-successfully-detects-b-c-earthquake/>). The 5 stations in our first-generation array were deployed for our first test project in 2017. Our first-generation stations used a next unit of computing (NUC) with Windows to run the system, which resulted in unforeseen issues. Subsequently, we converted the system to run on advanced RISC (reduced instruction

set computer) machine (ARM) processors running Linux, which had the added benefit of reducing our power consumption. Our first-generation stations used *Tetra* 2 microelectromechanical systems (MEMS) accelerometers custom-built by the late Dr. Kent Johansen, who was a brilliant engineer responsible for the design and construction of our first-generation stations. With the devastating loss of Dr. Johansen, our second-generation stations used the digital output ADXL355, 3-axis accelerometers (data sheet on ADXL355 available at https://www.analog.com/media/en/technical-documentation/data-sheets/adxl354_adxl355.pdf). While the digital noise from the commercial accelerometers is consistent with the *Tetra* 2, we recognized during our early deployments in 2017 that our detection level was higher than we anticipated. Our sensors exceed the BCOGC's specifications for ground motion monitoring in the Kiskatinaw Seismic Monitoring and Mitigation Area (KSMMA), which requires reporting of events with ground motion of 0.8 %g or greater or that are felt. However, while our sensors detect all signals above 0.03 %g, equivalent to all M 1.5 events within 15 km, which is sufficient for current traffic-light protocols (TLP) in the Montney, the detection of operationally-induced events requires a denser array than the 15 stations we initially proposed. As data on operationally-induced events are critical to research on AIS and these data are not available anywhere else, it was necessary to redesign our initially proposed array. As opposed to expanding our accelerograph array, we recognized that we could detect a greater number of lower magnitude, operationally-induced events by adding 3C commercial geophones to our existing array. However, without the expertise of Dr. Johansen, the station upgrades and the addition of the geophones required a significant amount of time, delaying the construction of our final array.

The stations in our array are powered by a solar panel with an absorbent glass mat (AGM), deep cycle battery. The data is stored on ultra-high capacity USB drives connected to the ARM processors, which are stored within protective (weather and animal proof) cases. The protective case also encloses a global positioning system (GPS) for timing and station location. Telemetry is currently provided by cellphone modems with antennas and in some cases machine-to-machine (M2M) cellphone boosters to improve the signal. We are ongoing investigating using Satellite M2M systems to provide telemetry in more remote locations. The solar panels are mounted on an in-house designed aluminum frame, which we have recently upgraded to include a raised, covered shelf to enclose the protective case and batteries off the ground (Figure 1). The accelerometers are enclosed in sealed tubes, 50-80 cm in length and 7.5 cm in diameter that are buried under surficial alluvium with a shovel or post hole digger to depths of 30-120 cm. The commercial, 3C, 5 Hz geophones are either in conical, marsh cases or in surface cases, 11x9x6 cm boxes with three metal bottom spikes, which are shallowly buried (~30 cm). Our surface and marsh 3C geophones have the same sensor elements and have identical specifications, apart from the case design. The element specifications are provided in Appendix 1. We custom designed and printed the amplifier circuit boards for the geophones based on adapting an existing design

(<https://github.com/olewolf/geophone/blob/master/Amplifier%20Schematic.pdf>). We used a commercial board for the analog to digital conversion (https://www.waveshare.com/wiki/High-Precision_AD/DA_Board). The boards are mounted within the protective cases. The station design is illustrated with labeled photos and a schematic diagram in Figure 2. The stations are robust and, without interference (ex. theft, rodents), can remain operational for years. One accelerograph station installed to monitor a disposal well has been running without maintenance since 2018.



Figure 1. The evolution of our solar panel stand design from left to right.

The raw data is collected and stored at 250 Hz for the accelerometers and 500 Hz for the geophones. When data is recorded above a set threshold, an alert is emailed through a real time cellular connection and the data is transferred to our server. Our server then automatically transfers the geophone data to our SeisComP3 system while the accelerometer data is transferred to our online, interactive platform, Portae Terra.

Accelerographs

Our telemetered stations provide real-time accelerometer data to an online interactive platform, Portae Terra (www.portaeterra.ca). When new data is received by our server, once an alert has been triggered, the raw data is automatically transferred to Portae Terra. Proprietary data is selectively available to operators through a unique passcode to access Portae Terra. Once data is received, Portae Terra removes the instrument response and calculates ground motion parameters, including the maximum amplitude for the peak ground acceleration (PGA) for the vertical component and the geometric mean of the horizontal components, the peak ground velocity (PGV), and peak ground displacement (PGD). Additionally, the

spectral intensity (SI), which provides a measure of the damage potential to structures by events, is calculated according to Rosenberger (2010). The corrected waveforms and calculated parameters can be viewed in Portae Terra and a download option is also available, which provides a zipped folder containing CSV files with the data in μg and cm/s^2 , the calculated ground motion parameters, and the calculated response spectral accelerations (PSA) at periods of 0.05, 0.1, 0.3, 0.5, 1.0, 2.0 and 3.0 s. The zipped folder also contains the raw data in miniSEED format and the dataless SEED volume for the station. While the data is not available to the public, due to confidentiality, access can be granted with permission (contact the lead author).

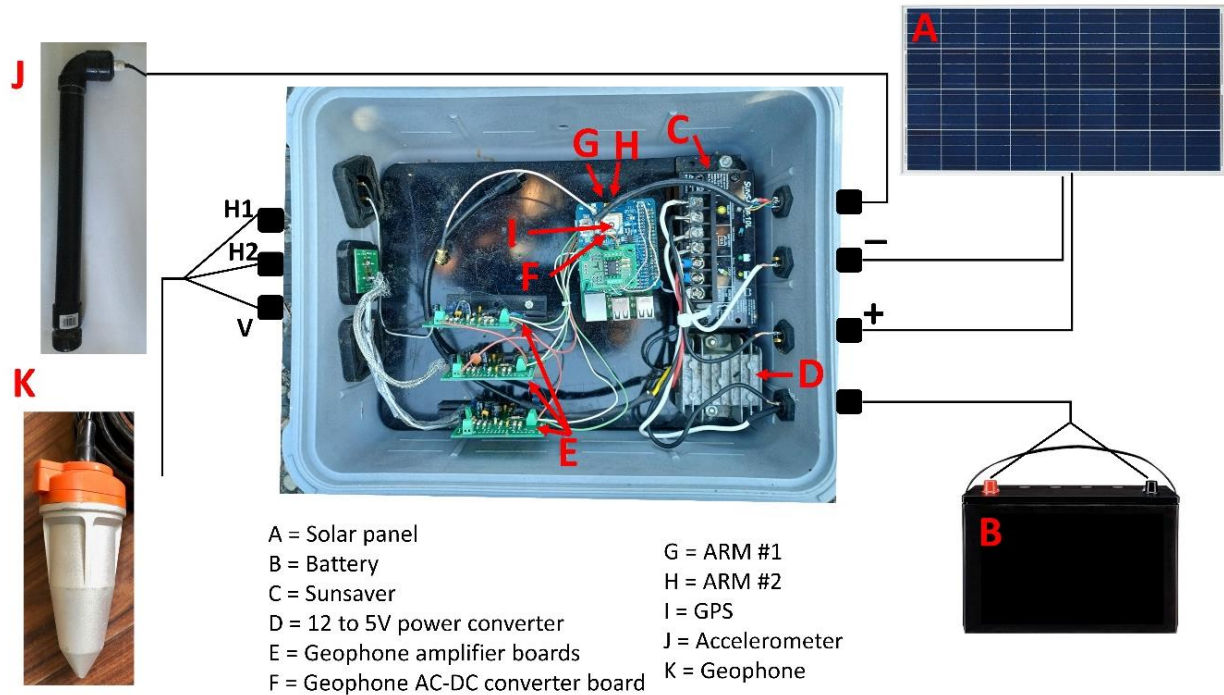


Figure 2. Schematic diagram illustrating the components of our station design. Note that ARM #2 (H) is mounted on top of ARM #1 (G) and that the geophone AC to DC converter board (F) is underneath the GPS (I). Not to scale.

A simple amplitude threshold is used for event detection. More sophisticated auto-detection techniques were investigated (see Li et al., 2018 for a summary); however, the heavy contamination of the recordings at all our stations from large-amplitude animal and anthropogenic noise makes auto-discrimination of seismic events difficult. In particular, seismic events recorded on single stations are difficult to discriminate from noise when the amplitudes are close to the digital noise ($0.2 \text{ cm}/\text{s}^2$ [$0.02 \%g$] for geometric mean of the horizontal components and $0.4 \text{ cm}/\text{s}^2$ [$0.04 \%g$] for the vertical component).

Dataset

From 2018-2019, our accelerographs were deployed at 29 sites across Western Canada. Our stations have provided the BCOGC required ground motion monitoring for 8 hydraulic fracturing operations and three disposal wells in the Montney. While monitoring disposal operations was outside the original scope of the project, the monitoring provided additional testing of our accelerographs and was necessary to maintain our working relationship with an operator. Seven of the 8 hydraulic fracturing operations were in active areas of induced seismicity within the KSMMA, which requires reporting of events with ground motion of 0.8 %g or greater, or that are felt. This provides confirmation that one of our accelerographs can be used in place of a force-balance accelerometer (FBA). Details on the 8 hydraulic fracturing operations, including the number of stations and the sensors used, are summarized in Table 1.

Table 1. Summary of the 8 hydraulic fracturing monitoring operations.

Year	Operation	Site ID	# Accel	# Geo	# events	Comments
2018	1	04	1	0	0	Small frac
	1-2	04	1	0	2	
		13	1	0		
	2	13	1	0	6	
	3	03	1	0	4	
	4	02	1	0	0	Inactive area
	5	13	4	0	3	Small frac
	6	13	1	0	18	Site 13 offline for part of frac
		16	1	0		Sites 13 and 16 are ~1 km apart
	6-7	13	1	0	5	
		16	1	0		
2019	7	13	1	1	26	
		16	1	0		
2020	8	16	1	1	8	Medium frac
		17	1	1		Site 17 offline for half of frac
	18	1	1			
	19	1	1			Site 19 offline for most of frac
	20	1	1			
	21	1	1			
	22	1	1			
	23	1	1			
	25	1	1			

Accel = accelerometers; Geo = geophones; Small frac = less than 7 days of injection; Medium frac = less than 14 days of injection.

The first five hydraulic fracturing operations were monitored with a single accelerograph station while the following two were monitored with two accelerographs deployed within ~1 km of each other. For the seventh operation, we upgraded one of two deployed accelerographs to the first of our paired stations with both an accelerometer and a geophone. Although we completed upgrading our stations to include geophones early in 2020, due to the downturn in industry activity related to the drop in oil price in addition to delays related to the current coronavirus pandemic (aka. COVID-19 pandemic), only one dense monitoring project was undertaken (Fall, 2020).

One of our goals was to demonstrate that the data from our accelerometers could be used to obtain accurate locations for events with $M>1.5$, whereas our geophones could be used to obtain solutions for events with $M<1.5$. The deployments for our first 7 operations, during the testing of our accelerographs, did not provide the necessary coverage to locate events. While four events were detected by 3 or more accelerometers during our dense monitoring project, they were all to the east of our array, providing poor azimuthal coverage. Thus, only ground motion data is reported from our accelerometers. For comparison with our ground motion data, we were provided confidential access to solutions from some of the events reported by a local operator-deployed broadband array. Solutions are only reported for events with $M>1.5$ from the local broadband array, as the location accuracy is too poor for smaller events. To conserve confidentiality, locations and times of events have been omitted from this report. Event solutions reported by NRCan and Visser et al. (2020), when available, were also included for comparisons with our data.

During our deployments, a total of 73 events with magnitudes from 1.5 to 4.5 were recorded by our accelerometers with pre-site corrected PGA (for geometric mean of horizontal components) ranging from 0.030 %g (0.29 cm/s²) to 8.1 %g (79 cm/s²) for hypocentral distances of 1.2 to 28.3 km. The recorded events are listed in Appendix 2 by operation. The station site ID, the site-corrected PGA (for geometric mean of horizontal components), and the site-source distance are also included in the table in Appendix 2, in addition to the magnitudes, when available, from the local broadband array, NRCan, and Visser et al. (2020).

No events were detected on the first operation in 2018, which was a comparatively small frac (>7 days of injection), while 6 events with M_w between 1.5 and 1.9 were recorded during operation #2 (site 13) and 4 events with M_w between 1.6 and 1.8 were recorded during operations #3 (site 03). One event, recorded by the local operator-deployed broadband array, was not detectable above the digital noise of our accelerometers for both operations. Operation #2 missed a M_w 1.7 event, 5.1 km away and operation #3 missed a M_w 1.5 event, 0.7 km away. Operation #4 was the only monitoring project outside the KSMMA, and no events were detected. Operation #5, which was the smallest hydraulic fracturing

operation we monitored, induced 3 events, which were detected by our station (*13*). The largest event, a M_w 2.0 was the first event recorded and was followed by two M_w 1.6 events. During operation #6, 18 events were detected by our stations, including 2 red-light event (M_L 3.9 and 4.5). Two stations (*13* and *16*) were deployed ~1 km apart to monitor operation #6; however, one of the stations (*13*) was damaged by a deer and not operating for two days, during which time 13 of the 18 events were missed, including both red-light events. The first red-light event, the largest event in the sequence, was preceded by 2 green-light events ($M < 2$) and was followed by the second red-light event and 5 yellow-light events ($M 2-3$). Operations #6 and #7 were on neighbouring pads and the same sites (*13* and *16*) were used to monitor both operations. A greater number of anomalous events were induced by operation #7 than #6; however, only 3 yellow-light events were induced, the largest, a M_w 2.4 event early in the sequence. One M_w 1.5 event, detected by the local, operator-deployed array, was missed by our sensors during operation #6 and one event with $M_w < 1.5$, which was not reported from the local broadband array was detected. All the events reported from the local broadband array for operation #7, were detected by our stations and an additional 14 events, not reported by the local broadband array, were detected. During pre- and post-completions monitoring, an additional seven events were detected in 2018 and 2019.

Our first dense monitoring project was recently completed (Fall, 2020). Due to timing and logistical constraints imposed by the pandemic we were only given three weeks preparation time before the start of the hydraulic fracturing operation. As a result, we were unable to complete a prior site investigation, the installations were of necessity rushed, and station maintenance was limited. Additionally, we did not have the time to obtain permits or permissions for site access and could only find locations for 9 of our 15 paired stations and some of the stations were poorly located for azimuthal coverage. Further, two of the nine accelerometers were not operational for much of the deployment, due to technical issues resulting from rodent damage. While the deployment was not ideal, due to the ongoing pandemic and travel restrictions, we were uncertain when or if another opportunity would be available. The locations of the stations with respect to the pad that was completed are shown in Figure 3. Stations *17* and *19* were not operating at the time of all nine events. Station 23 was operational but was too distant from all events to detect any signals above digital noise.

Although the operation we set out to monitor was a relatively small hydraulic completion (12 days of injection; pad 1), a larger completion started the day prior on a pad ~7 km to the southeast (21 days of injection; pad 2), which was immediately followed by a smaller operation on a neighbouring pad (6 days of injection, pad 3). Additionally, a 4th hydraulic fracturing operation was completed at the same time, 26 km southeast from the pad we were monitoring (pad 4).

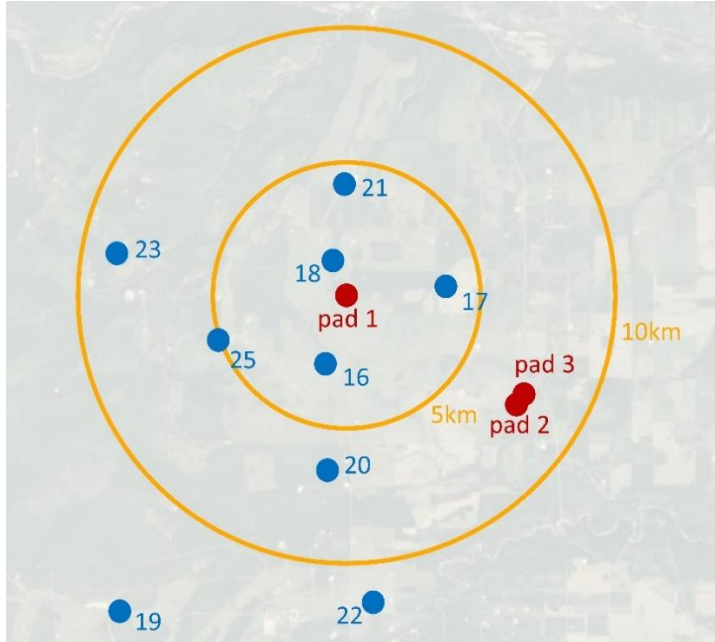


Figure 3. The locations of our 9 stations (blue circles) deployed for the dense monitoring of a hydraulic fracturing operation on pad 1, whose location is shown by the center red circle. The locations of the nearby hydraulic fracturing operations on pad 2 and pad 3 are also shown by red circles. Circles with radii of 5 and 10 km are shown on the map for scale. Additional location identifiers are intentionally omitted to preserve confidentiality.

The site corrected PGA (for geometric mean of horizontal components), hypocentral distances, and magnitudes, when available, for the nine events detected during the dense deployment are tabulated in Appendix 2 and the locations for the events are presented in Figure 18 in the Geophone Section of this report. Two events were recorded by the accelerometers during the time of the operation on pad 1 (events A and B), the pad we were monitoring, and 7 events were recorded afterwards, the latest of which (event I) occurred after all four hydraulic fracturing operations had completed injection. Eight of the 9 events were located to the east of our array (not event H); two occurred to the north-east of pad 1 (E and G), four occurred between pad 1 and pads 2 and 3 (A, B, C, and I), and two occurred close to pad 4 (D and F). The two events near pad 4 (C and E), were the largest recorded. The smallest four eastern events all locate closest to pad 1, while the M>2.0 events B and C were located closer to the pad 2 operation occurring at the same time. Event H was the smallest event detected (M<1.5) by our accelerometers, it occurred 11 days post-injection of pad 1 and was the only detected event west of pad 1. Event H was not reported by the local operator-deployed broadband array, surprisingly, nor was event C, even though it was larger than event B (i.e., the other M>2 event not associated with pad 4). While we were provided initial solutions for the events from the local broadband array, in order to conserve confidentiality for this

report, we have only compared their reprocessed solutions for two events (B and E). The locations will be discussed further in the Geophones section.

All M>1.5 events, which occurred during our monitoring operation, were located to the east of our array, which exposed our poor azimuthal coverage, in particular due to the failure of station 17, our only eastern station. As a result, only four of the events were recorded by four or more stations (B, C, E and F), one was recorded by three stations (H), two were recorded by two stations (G and I), and two were recorded by one station (A and D). The recorded pre-site corrected PGA (for geometric mean of horizontal components) for the nine events range from 0.035 %g to 0.23 %g (0.35 cm/s² to 2.3 cm/s²).

Site Corrections

The measured PGA were corrected for events recorded by our accelerometers to a reference site class with a time-averaged shear-wave velocity over the top 30 m (V_{s30}) of 760 m/s using the amplification factors from Seyhan and Stewart (2014) following the method described by Babaie Mahani and Kao (2018). In the first step, we calculated the response spectral acceleration (PSA) at frequencies from 0.1 to 100 Hz for the geometric mean of the horizontal components and the vertical component. The spectral ratio of the horizontal-to-vertical components (H/V) is then calculated for each event, following which the H/V ratios are log-averaged for each station. The fundamental frequency (f_{peak}) was then defined as the frequency at the peak H/V amplitude. Using the correlation of Hassani and Atkinson (2016), V_{s30} were estimated from f_{peak} for each station with recorded events. The class for each site could then be determined from V_{s30} based on the classification of the National Earthquake Hazards Reduction Program (NEHRP), which could then be used to determine the PGA correction factor (F_{PGA}). The site class could only be determined for those stations that recorded multiple events. Following correction, the PGA (for the geometric mean of the horizontal components) for our events range from 0.02 7%g to 8. 1%g (0.26 cm/s² to 78 cm/s²). The V_{s30} , f_{peak} , site class, and F_{PGA} for our stations are shown in Table 2. The corrected PGA, as well as the event magnitude and hypocentral distance when available are shown in Appendix 2.

Attenuation

The site-corrected PGA versus hypocentral distance for events recorded by our stations were overlain on the data and predictive model presented for the South Montney by Babaie Mahani and Kao (2018). The results, which are plotted in Figure 4, show the datasets are consistent. However, our PGA for some events are higher than predicted by the ground motion prediction equation (GMPE). This may be a result of our simple method for correcting site effects (i.e., amplification), that we are using a combination of local and regional solutions, and/or due to asymmetrical radiation resulting from rupture directivity. The

plot also shows our minimum threshold for detection as a result of our digital noise. The MEMS sensors we are currently deploying allow detection of events with $\text{PGA} > \sim 0.03 \text{ %g}$.

Table 2. The f_{peak} , V_{s30} , site class, and F_{PGA} for our stations with recorded events.

Site ID	f_{peak} (Hz)	V_{s30} (m/s)	Class	F_{PGA}
13	10.52	698.0	C	1.3
04	8.33	602.6	C	1.3
03	8.33	602.6	C	1.3
16	13.33	810.3	B	0.9
18	10.52	698.0	C	1.3
20	13.33	810.3	B	0.9
22	13.33	810.3	B	0.9

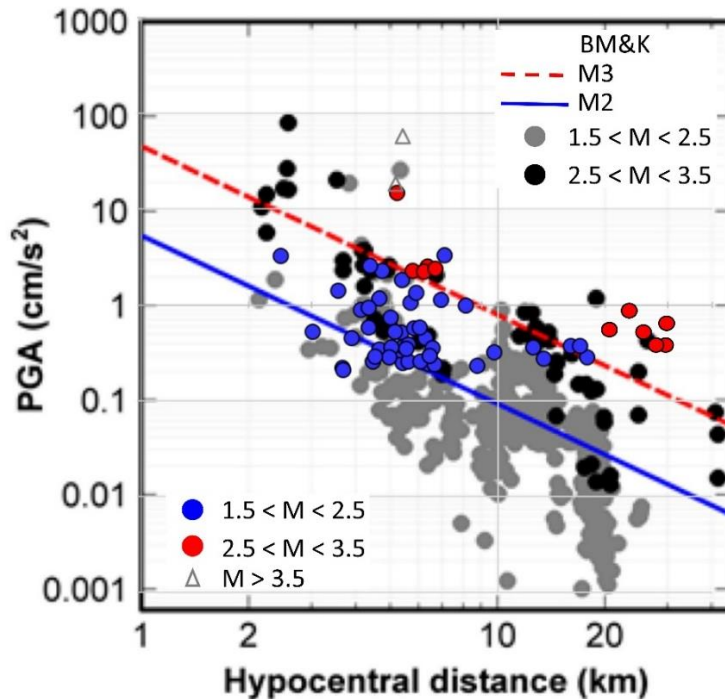


Figure 4. Site-corrected PGA versus hypocentral distance for events recorded by our array with $1.5 < M < 2.5$ plotted as blue dots, $2.5 < M < 3.5$ plotted as red dots, and $M > 3.5$ plotted as grey triangles overlaid on GMPE (red dashed line = M3; blue solid line = M2) and data (gray dots = $1.5 < M < 2.5$; black dots = $2.5 < M < 3.5$) from Babaie Mahani and Kao, (2017; BM&K).

Magnitude of Completeness

To investigate the magnitude of completeness for our sensors, we have plotted the magnitude versus hypocentral distance for events that were detected by one or more of our stations (blue) and events that

were not (grey; Figure 5). The results indicate that $M>1.5$ events are consistently detected within $\sim 15\text{km}$ of our stations, $M>2.5$ events within $\sim 22\text{ km}$, and $M>3$ within $\sim 30\text{ km}$.

We are detecting events with $M<1.5$, however we did not have access to information for these events as the data from the local, operator-deployed array, which we were provided some confidential access to, does not provide sufficient solutions for such small events. This information is now available from our stations through their upgrade to include 3C geophones. However, due to the rushed deployment, the geophone sensors were not adequately installed, and all tilted significantly due to soggy ground conditions, providing inaccurate amplitudes unsuitable for magnitude calculations (discussed further in the Geophones section).

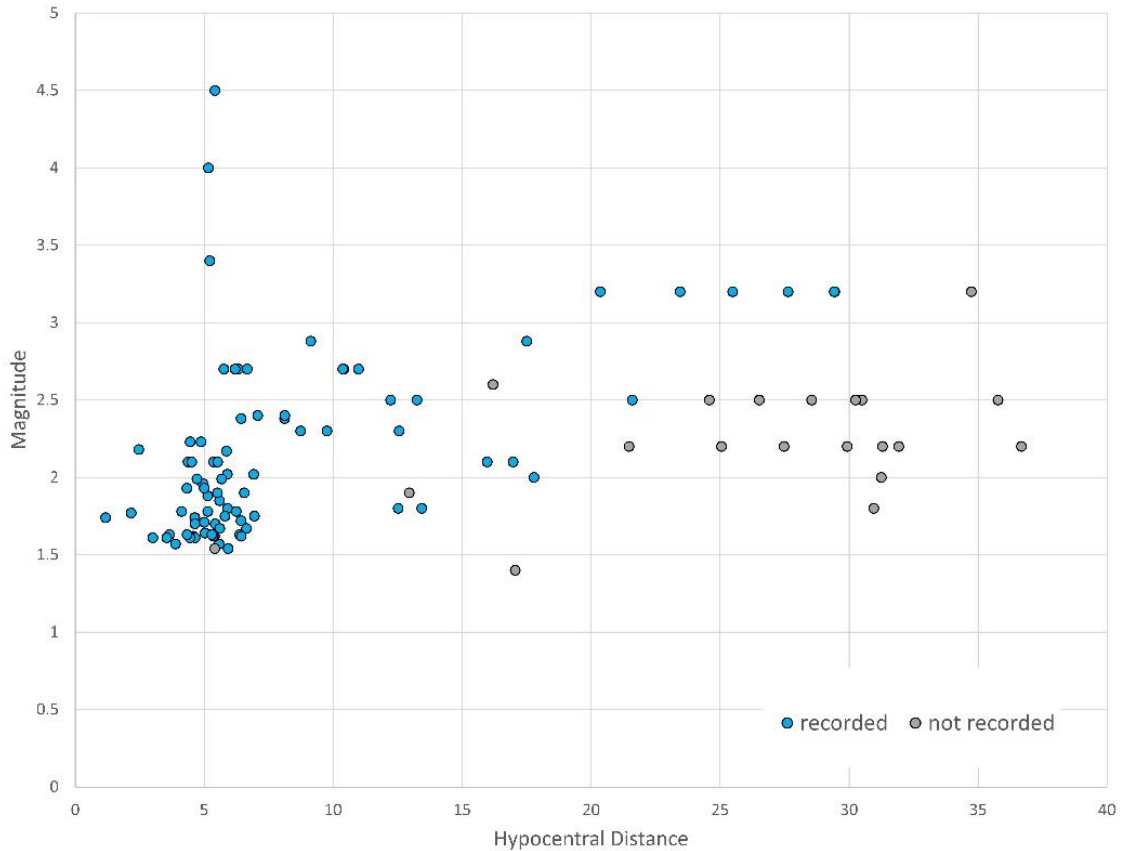


Figure 5. Magnitude (M_L and M_w) versus hypocentral distance (in km) for events which were detected on our stations (blue) and were not detected on our stations (gray).

Our data plotted in Figure 5 shows two outliers. In particular, based on its magnitude and hypocentral distance, the $M_L2.6$ event on January 19, 2019, reported by NRCan, should have had sufficient ground motions to be detected by our sensors. At the time of the event (between operations #5

and #6), two stations where deployed ~1 km apart and ~16 km from the event. In comparison, two smaller events with similar hypocentral distances (operation 5-6, event #1 18 km, M_L 2.0, and event #5 17 km, M_L 2.1) show clear P- and S-wave arrivals and the larger event does not (Figure 6). A denser array of accelerometers would have been required to understand why this event was not recorded. A possible explanation is that the M_L 2.6 event has a source which radiated asymmetrically with a minimum axis in the direction of our stations. Strong evidence supporting this hypothesis is provided by the results of our recent dense monitoring project. As discussed further in the Rupture Directivity section, the ground motions recorded by our stations for some events show asymmetrical radiation patterns.

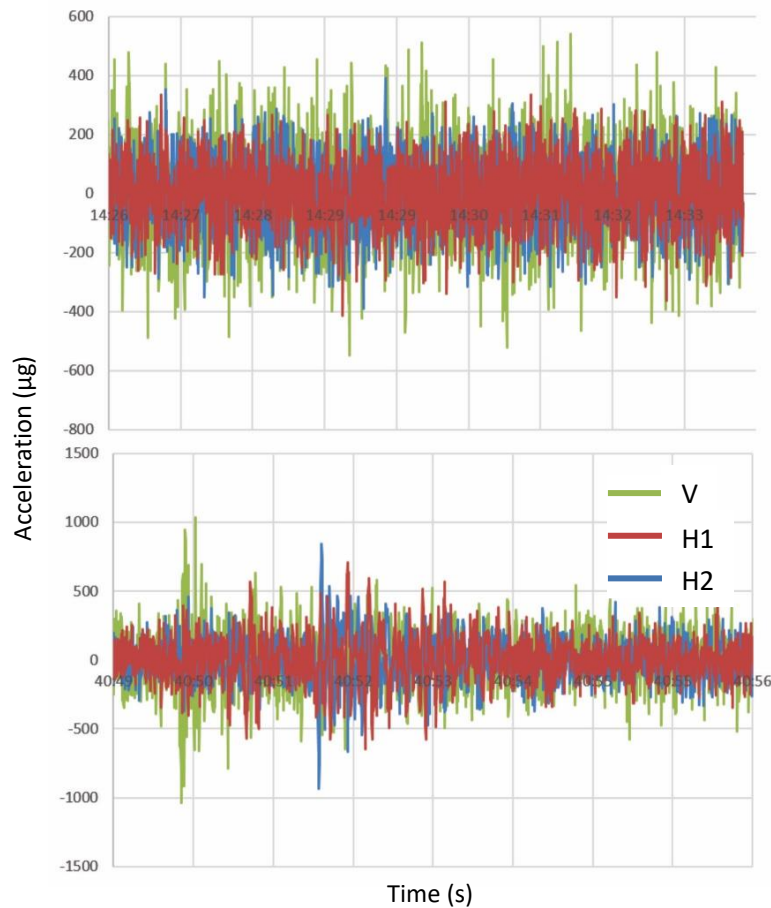


Figure 6. (top) Data recorded on one of our accelerometers at the time of the M_L 2.6 event on Jan. 19, 2019, reported by NRCan (16 km hypocentral distance from station) compared to (bottom) data recorded on the same station from the M_L 2.1 event #5 from operation 5-6 (17 km hypocentral distance).

Depth of Burial

The digital noise on our accelerometers is very consistent and never produces significant peaks followed by significant troughs. The digital noise is considerably greater than the background noise of a FBA;

however, any signal above 0.03 %g is detected, which is well below the threshold for felt events. All our accelerometers experience some amount of animal and anthropogenic noise, which is either of very long duration (ex. machine, or vehicle) or very short duration with multiple bursts, some with very high amplitude (ex. animals, people). Such noise had little impact on the results, other than producing false threshold alerts. In order to avoid animal and anthropogenic noise, we would have to bury our sensors very deeply, requiring a drill rig. As the purpose of the array is to be inexpensive, temporary, and easily deployable, burying our sensors at such depths was thus outside the funding and scope of this project.

To investigate any possible impacts depth of burial and minor tilt variations of our sensors might have on recorded ground motions, we installed four sensors at different depths (30, 60, 90, and 120 cm) at a single site in a seismically active area for a 3-month period. The sensors were a maximum of 5 m apart with the 30 and 90 cm sensors and the 60 and 120 cm sensors within 1 m of each other. Eighteen events were recorded during the time of the deployment; however, two of the four stations experienced technical issues resulting from large animal damage and only 6 of the events were recorded on 3 or more stations. As shown by the normalized difference between the PGA (geometric mean of the horizontal components) recorded on each station and the average value for the 6 events, presented in Table 3, no correlation was observed between sensor depth and PGA.

Table 3. The normalized difference between the PGA (geometric mean of the horizontal components in cm/s^2) recorded on the 4 sensors buried at different depths (30, 60, 90, and 120 cm) and the average value recorded on the sensors.

Event	30cm	60cm	90cm	120cm
1	-0.020	0.0079	0.012	
2	-0.20	0.094	0.12	-0.012
3	0.075	-0.019	-0.10	0.044
4		0.026	-0.041	0.015
5	-0.0078	0.020	-0.013	
6	0.041	0.0052	-0.046	

Rupture Directivity

Seismic waves are often assumed to propagate symmetrically from a circular source, with azimuthal variations averaging out. However, seismic wave interference due to rupture propagation may result in asymmetrical radiation patterns where ground motions depend on the azimuth from the source with higher amplitude and shorter duration ground motions in the forward propagating direction (Haskell, 1964).

Rupture directivity effects can thus result in recorded ground motions significantly higher than the median value predicted by GMPE at some azimuths, influencing the distribution of seismic hazard. The effects of

rupture directivity were observed by Holmgren et al. (2019) in more than one-third of the fluid-injection induced earthquakes they studied in the Western Canadian Sedimentary Basin. Determining the hazard from induced seismicity thus requires an understanding of the effects of rupture directivity, which is difficult in regions with sparse station coverage.

Four of the nine events recorded by the accelerometers in our dense monitoring array were detected by more than 3 stations. The largest of the four was a M_w 2.8 event located ~25 km from our stations (event F) and was recorded by 6 of the 7 accelerometers functioning at the time. The accelerograms for the 6 stations from the event, plotted on Portae Terra, are shown in Figure 7. The PGA calculated at each station is plotted in Figure 8. The results show ground motions highest closest to the event with values decreasing with increasing hypocentral distance as the energy attenuates.

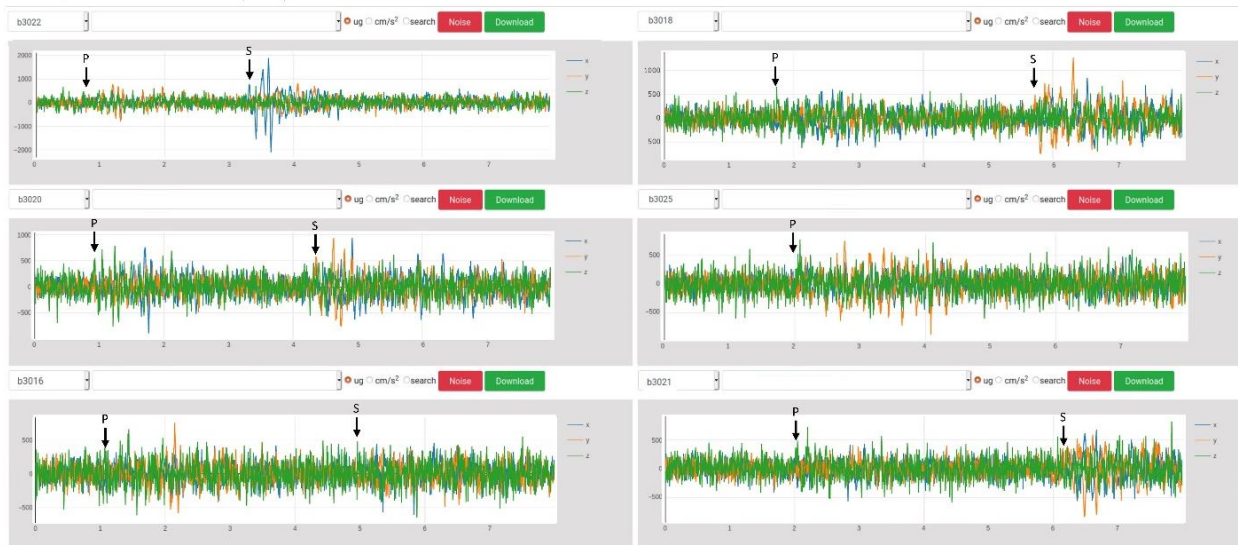


Figure 7. Ground accelerations (in μg) from a M_w 2.8 event (event F) recorded on 6 of our stations plotted on Portae Terra. The time of the first P- and S-wave arrivals are marked by arrows.

The accelerograms and calculated PGA are also presented for the two smallest events (B and E) recorded on 4 stations (Figures 9-12). While most of our calculated PGA fit within the anticipated scatter of the attenuation model, for example, the M_w 2.8 event presented in Figure 8, the ground motions for the two smaller events show distinct asymmetry, suggesting rupture directivity effects. Both events also similarly attenuated more quickly to the west than the south. Unfortunately, our eastern station, 17, was not operational at the time of either event, so the map, and thus our understanding of the ground motion attenuation, is not complete.

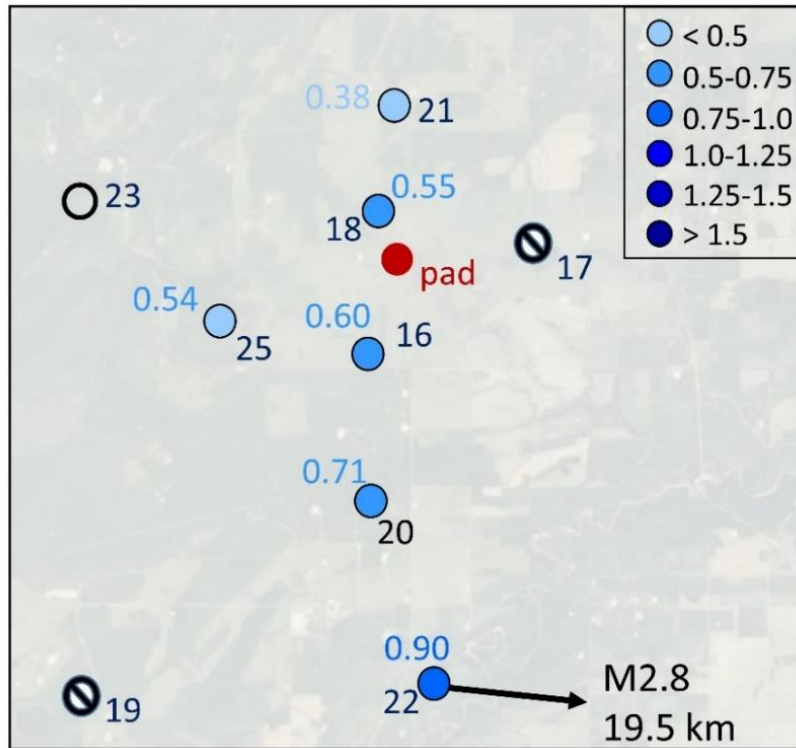


Figure 8. PGA (site corrected geometric-mean of the horizontal components; in cm/s^2) from event in Figure 7 (event F) recorded on our stations. Circles with a line indicate offline stations and open circles are stations with no detectable recording of the event.

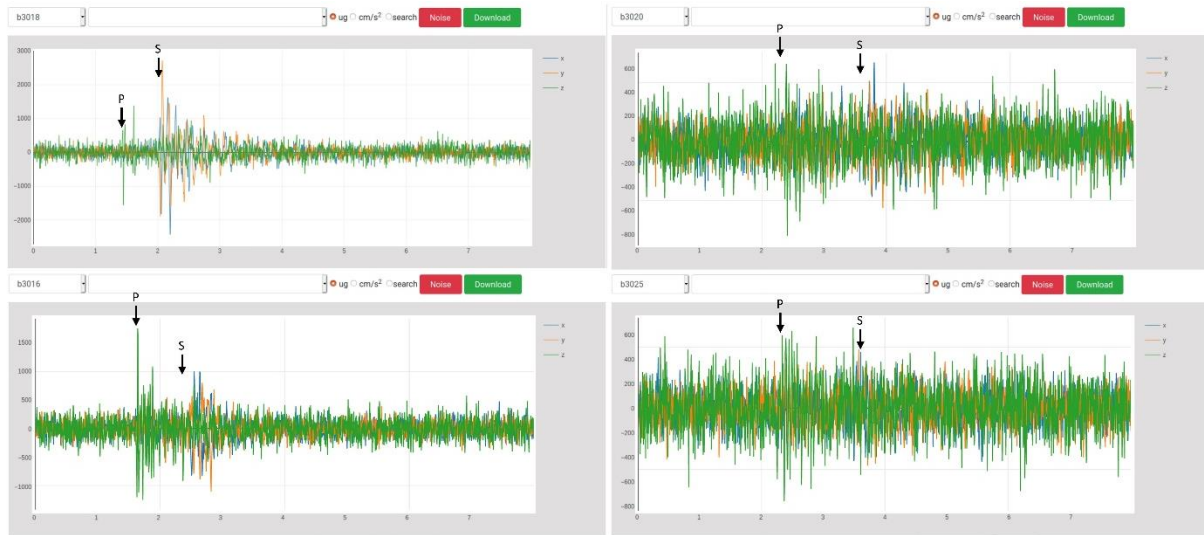


Figure 9. Ground accelerations (in μg) from event B recorded on 4 of our stations plotted on Portae Terra. The time of the first P- and S-wave arrivals are marked by arrows.

Figures 9 and 10 show the results for a M_w 2.0 event located 5 km east of site 16 (event B). The PGA recorded for the event on stations 18, 16, 20, and 22 are higher than expected from the ground motion attenuation model. While the signals are weak compared to the digital noise for 18 and 22, both P- and S-waves are apparent on stations 16 and 20. The difference in PGA recorded by stations 16 and 20 is much greater than predicted by their difference in hypocentral distance (16 is 4.9 km from event and 20 is 6.1 km). According to the attenuation model, the PGA for these stations should only vary by $\sim 0.1 \text{ cm/s}^2$ not 0.4 cm/s^2 . Additionally, site 20 is only 180 m closer to the event than site 18, yet their stations recorded quite different signals.

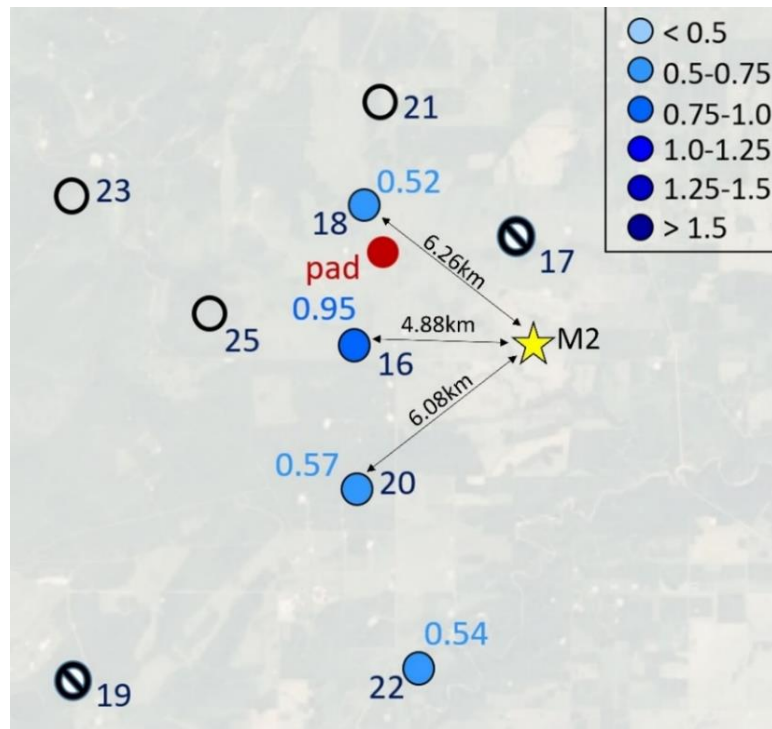


Figure 10. PGA (site corrected geometric-mean of the horizontal components; in cm/s^2) from event in Figure 9 (event B) recorded on our stations. Circles with a line indicate offline stations and open circles are stations with no detectable recording of the event. Yellow star indicates location of the epicenter.

The asymmetry is more dramatic for the M_w 1.7 event (event E), located 2.5 km east-southeast from site 18, presented in Figures 11 and 12. The PGA recorded at stations 18 and 16 are relatively consistent with the ground motion attenuation model (16 is slightly high), but station 21, which is only 71 m further from the event than station 16, did not record a signal above the digital noise. There was nothing unusual about station 21 that would explain why it did not detect this event. The noise was at the digital level (i.e., no anthropogenic or animal noise was recorded), the site elevation and conditions were the same as the other stations, and it did record a signal for the M_w 2.8 event. We do not believe site

effects nor noise can explain why station 21 did not record the event while a station only 71 m closer to the event recorded clear P- and S-arrivals and a PGA higher than expected from the attenuation models. Thus, we suggest the recorded asymmetrical PGA data is a result of asymmetrical radiation resulting from the source mechanisms

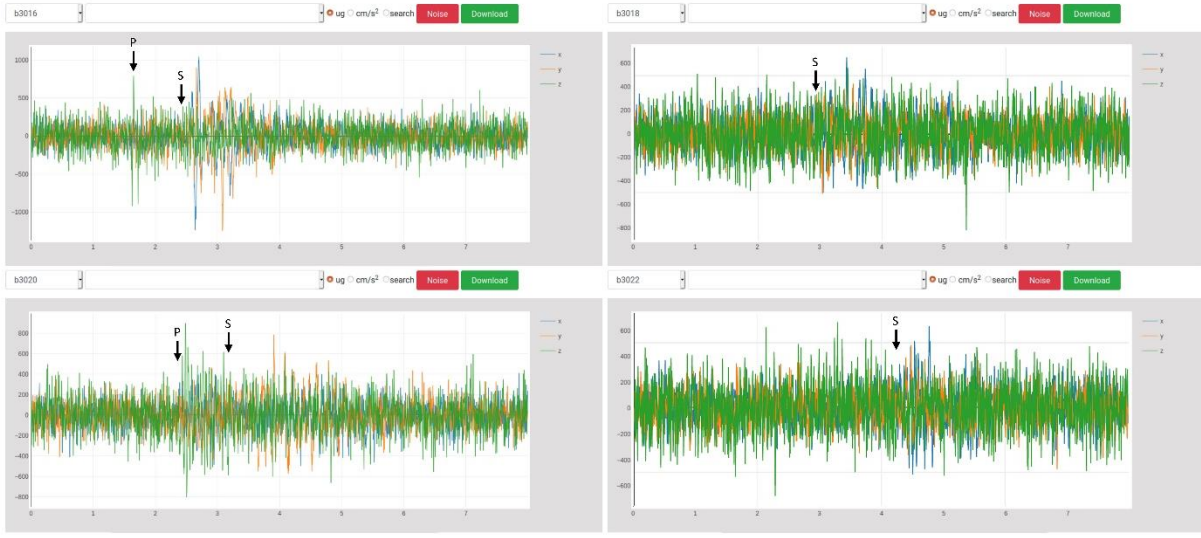


Figure 11. Ground accelerations (in μg) from event E recorded on 4 of our stations plotted on Portae Terra. The time of the first P- and S-wave arrivals are marked by arrows.

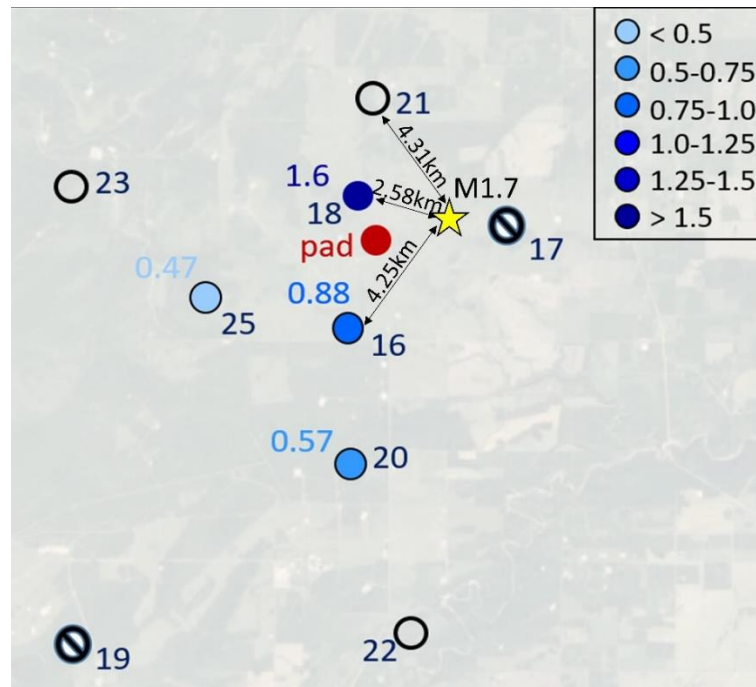


Figure 12. PGA (site corrected geometric-mean of the horizontal components; in cm/s^2) from event in Figure 11 (event E) recorded on our stations. Circles with a line indicate offline stations and open circles are stations with no detectable recording of the event. Yellow star indicates location of the epicenter.

Six of our seven operating accelerometers detected event C. Based on the data from nearby regional broadband stations (discussed further in the Geophones section), event C had a M_L 2.29 and was located 7.4 km east of station 20. The waveforms recorded by our accelerometers are shown in Figure 13 and the location of the event with respect to our array is plotted in Figure 14 along with the PGA recorded on the stations. As can be seen in Figure 13, the signals are quite different for stations 16 and 25, the 2 stations in the northwestern direction from the event, compared to the other four stations. While the P-waves are very prominent on stations 16 and 25, the S-waves are barely observable about the digital noise. In contrast, the P-waves are less prominent on the other four stations, while the S-waves are relatively large. As large S-waves were recorded on stations 16 and 25 for other events (ex. station 16 for event E in Figure 11), this is not a result of variations in station deployment. As a consequence of the smaller than anticipated S-waves on stations 16 and 25, the PGA for these stations, which were calculated from the geometric mean of the horizontal components (i.e., the PGA of the S-wave) are much lower than would be predicted from the GMPE. Further evidence for asymmetrical wave radiation is provided by comparing the signals from stations 20 and 22, which are essentially the same distance from the event, yet have quite different signals. While the S-wave and thus the PGA is higher for station 22 than 20, the P-wave is much smaller for station 22 than 20.

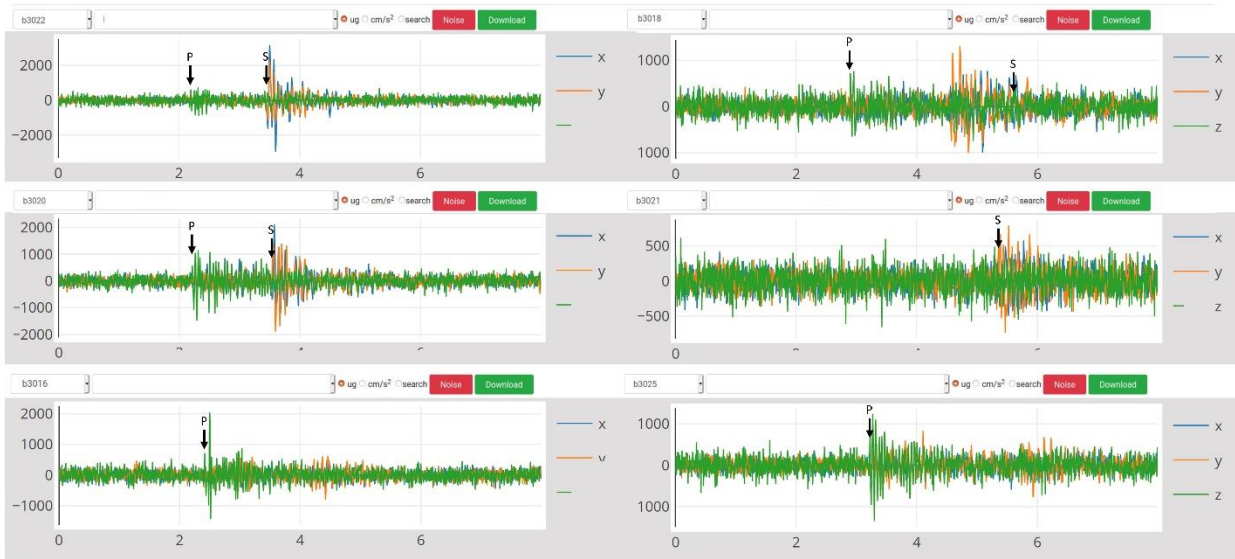


Figure 13. Ground accelerations (in μg) from event C recorded on 6 of our stations plotted on Portae Terra. The time of the first P- and S-wave arrivals are marked by arrows.

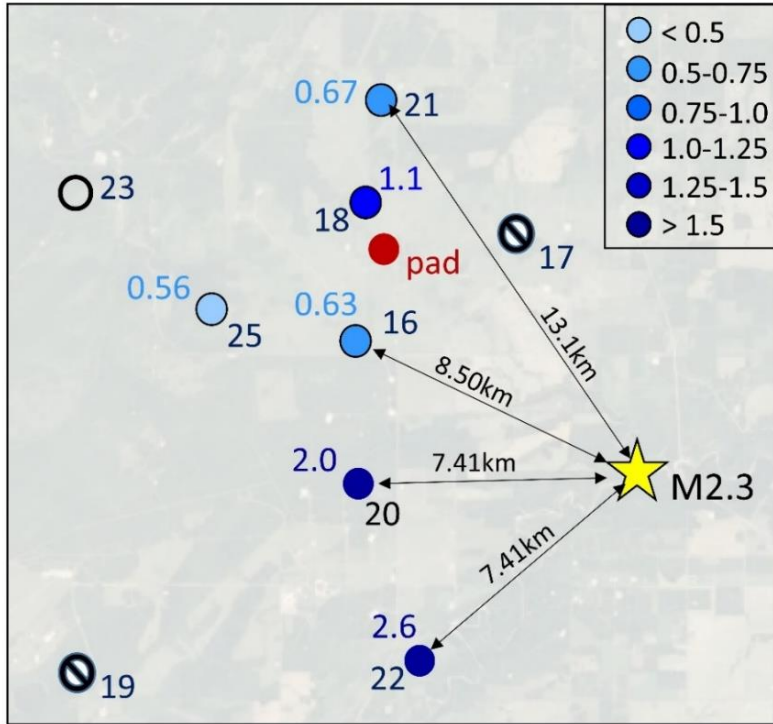


Figure 14. PGA (site corrected geometric-mean of the horizontal components; in cm/s^2) from event in Figure 13 (event C) recorded on our stations. Circles with a line indicate offline stations and open circles are stations with no detectable recording of the event. Yellow star indicates location of the epicenter.

Our monitoring results, as summarized above, suggest the need for increased ground motion monitoring and the use of dense arrays for monitoring, mitigating, assessing, and understanding the hazard posed by induced seismicity from hydraulic fracturing. Our array design provides a cost-effective means for undertaking such monitoring. For a fraction of the cost of a FBA, a magnitude more stations could be deployed providing a more detailed image of the induced ground motions. In addition to helping with research, a detailed distribution map of induced ground motions (i.e., ShakeMaps) will aid industry with public relations as stakeholders can visualize their risk from experienced or anticipated induced seismicity. The main disadvantage of our accelerometers is the higher detection threshold due to digital noise compared to a FBA; however, the detection threshold for our sensors is well below the threshold for felt ground accelerations. While it is incredibly important to have event solutions for operationally-induced events, ground motion parameters for events significantly lower than the threshold for felt events contributes little to our understanding of hazard (i.e., there is no anomalous induced event hazard). More sensitive accelerometers would be required for a ground motion based TLP with thresholds corresponding to $M < 1$ events. However, before such a TLP could be implemented, a much better understanding of the ground motions is required and how they relate to seismic hazard. Therefore, we argue that recording events with PGA at levels below the detection threshold of our sensors is not as important as

understanding the observed scatter with hypocentral distance, understanding rupture directivity, and understanding how the PGA relates to hazard. If the effects of rupture directivity are significant, *where* a single high-quality station is installed will impact the data, the calculated PGA may either be higher or lower than predicted from GMPE and if the attenuation is assumed to radiate symmetrical, the interpretation of the hazard would be incorrect.

Traffic-Light Protocols

At the time this project was first proposed, it was fairly well accepted that anomalous induced events were the result of pore pressure diffusion and as such traffic light protocols and probabilistic hazard maps would be effective. One of our objectives was to observe the increase in magnitude of events and the time lag between events predicted by a pore pressure diffusion model to develop a more effective TLP. However, since the study was proposed, many events have occurred which do not fit the pattern predicted by the pore pressure diffusion model. For example, the largest event we recorded, the only event with $M>4$ induced by hydraulic fracturing to date in the KSMMA (event #3 of operation #6) was not preceded by any yellow-light events ($M>2$) and occurred early in the sequence of events (#3 of 18 $M>1.5$ events). Similarly, the largest event induced by hydraulic fracturing to date in the Montney, a M_w 4.6 on August 17th, 2015, was also not preceded by yellow-light events. Therefore, the most hazardous events induced in the Montney did not follow the anticipated pore pressure diffusion model and could not have been mitigated by traffic light protocols. Additionally, some of the data from the operations we monitored do not follow the anticipated relationship between maximum magnitude and numbers of events. Two of the operations we monitored induced a larger number of $M>1.5$ events with lower maximum magnitude. Operation #7 induced 26 $M>1.5$ events with a maximum magnitude of 2.4 and we detected 56 $M>1.5$ events with a maximum magnitude of 3.2 for the completions on pad 4 during operation #8, whereas operation #6 induced 18 $M>1.5$ events with a maximum magnitude of 4.5.

A better understanding of the processes controlling the magnitude and number of anomalous events induced by hydraulic fracturing operations is needed before better mitigation and prevention frameworks can be developed. While TLPs are necessary in the interim, as discussed in the Scientific Review of Hydraulic Fracturing in British Columbia (Scientific Hydraulic Fracturing Review Panel, 2019), proactive solutions with a better understanding of the conceptual model(s) are required to replace TLPs. Similarly, probabilistic hazard maps can not be accurately developed without a better understanding of the conceptual model(s) as well as the cumulative effects from multiple operations occurring nearby in time and/or space. We believe the most pressing questions are understanding the mechanisms(s) controlling anomalous induced events and the resulting ground motions and how they

relate to hazard and risk, which requires information on operationally-induced seismicity and dense ground motion monitoring.

Geophones

Understanding the spatial-temporal and magnitude-frequency distribution of smaller magnitude events ($M < 1.5$) may be critical to enable proactive mitigation schemes to improve upon current TLPs. In addition, a distribution map of the smaller events provides the geometry of fractures and faults required for physics-based 3D modelling necessary to better understand and forecast anomalous induced seismicity. Monitoring for operationally-induced events may also provide important data on frac hits as well as an estimate of the reservoir volume stimulated by the hydraulic fracturing operation. Further, small broadband arrays are not effective in areas with regulated traffic-light magnitudes less than 1.5. We recognized this need for a more complete catalogue of events early in this study and therefore upgraded our 15 accelerograph stations to include commercial, high-precision, 5 Hz, 3C geophones. In order to obtain near-real time solutions for events detected by our geophone array, we developed an automated local monitoring system using the open-source program SeisComP 3 by Helmholtz Centre Potsdam GFZ German Research Centre for Geosciences and gempa GmbH (2008).

While geophones are good for small magnitude events ($M < 1.5$), their instrument response is unable to detect the low frequency content of larger magnitude events, resulting in an over-estimation of magnitudes (Yenier et al. 2017). While it is possible to use our accelerometer data to obtain solutions for larger magnitude events, the regional broadband network in NEBC is sufficient in many areas of the Montney to detect all events with $M > 1.5$. As regulated mitigation protocols (i.e., TLPs) are currently based on magnitude it is crucial for automatic solutions to be consistent with those reported by the regulators. Therefore, we set up a second, regional SeisComP system mimicking the approach of the British Columbia Oil and Gas Commission (BCOGC). Our second system uses data from regional broadband stations with real-time data available through IRIS (<https://www.iris.edu/hq/>) in combination with our geophone data. For this first test of our paired array, given our limited preparation time before the operation, we have used the default iasp91 velocity model and not a more accurate local velocity model as the operator-deployed local broadband array has employed. We calculate our magnitudes using the local magnitude calculation standard generated for the Western Canadian Sedimentary Basin (Babaie Mahani and Kao, 2020).

Both automated systems were employed for our dense monitoring project during a 14-day period encompassing the main hydraulic fracturing operation. Our geophones detected 323 operationally-induced events near our monitoring array. However, the installation of our dense array was rushed due to

the current pandemic and in combination with unseasonal, prolonged rainfall and poor ground conditions, the geophone sensors, in hindsight, were not adequately buried. As a result, most sensors tilted beyond their error limit contaminating our amplitudes and the resulting magnitude calculations. While some vertical components were of no use, due to the sensor tilt, the first P-wave arrivals are adequate on the horizontal components to be combined with picks on the vertical components of less contaminated stations to obtain locations for the events. As a consequence of picking P-arrivals on the horizontal component, some events were miss-located by our system due to S-arrivals miss-picked as P-arrivals. Our system also miss-associated arrivals from events that occurred very close together in time. In the future, scanloc will be purchased for use with SeisComP to improve results for clusters of events. The open source, SeisComP, used in our study, utilises a two-stage detector for picking P-waves and a phase associator that locates events based on the P-wave detection. While SeisComP is designed for large teleseismic events, scanloc is specifically designed to monitor for local and small to micro magnitude events. In scanloc, a cluster search algorithm is used to associate phase detections and both P and S-arrivals are used for locating events.

Once all events were checked for consistency and the necessary picks were adjusted, 335 operationally-induced events were located within our monitoring area. Examples of the waveforms from two typical small magnitude events (events 251 and 252) detected by our geophone array are included in Figure 15. The locations for the two events obtained from our system, displayed as screenshots, are included as Figures 16 and 17. The epicenters for all the operationally-induced events are plotted in Figure 18 as grey dots, with the locations for events 252 and 253 plotted as red dots and labelled. The epicenters for all the operationally-induced events with respect to pad 1 are also tabulated in Appendix 3. The majority of the events locate to the southwest of the pad, which is likely a consequence of our poor sensor coverage to the north-east, in particular as station 17 was only available for ~6 days of the operation. While we can see linear features in the clusters of events, it is difficult to conclusively map features as many of our locations are unreliable due to the unavailable vertical components and the poor azimuthal coverage of our array. However, our data is promising in that it shows that with our full 15 station array and more time for site selection and station deployment, we would likely have obtained sufficient data to map the major fracture network associated with the hydraulic fracturing operation.

In addition to the operationally-induced seismicity (magnitude approximately less than M_L 0.8), 26 larger magnitude anomalous induced events (approximately greater than M_L 0.8), were also located by our system, including events A and B detected by our accelerometers. Examples of three such events (185, 297, and 343), located by our system from our geophone array are presented in Figures 19-24.

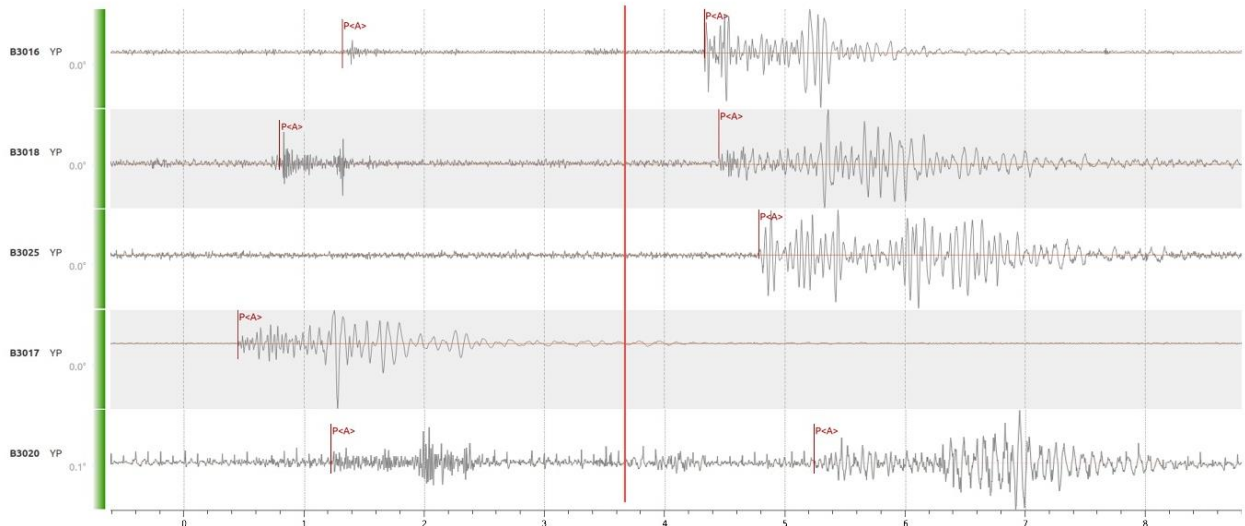


Figure 15. Waveforms for two typical operationally-induced events (252 and 253) recorded on our geophones. The component shown for each station is indicated in Figures 16 and 17. Small red arrows, labeled P<A>, indicate the automatic picks made by our system. Large red line indicates the event time for the second event shown (253).

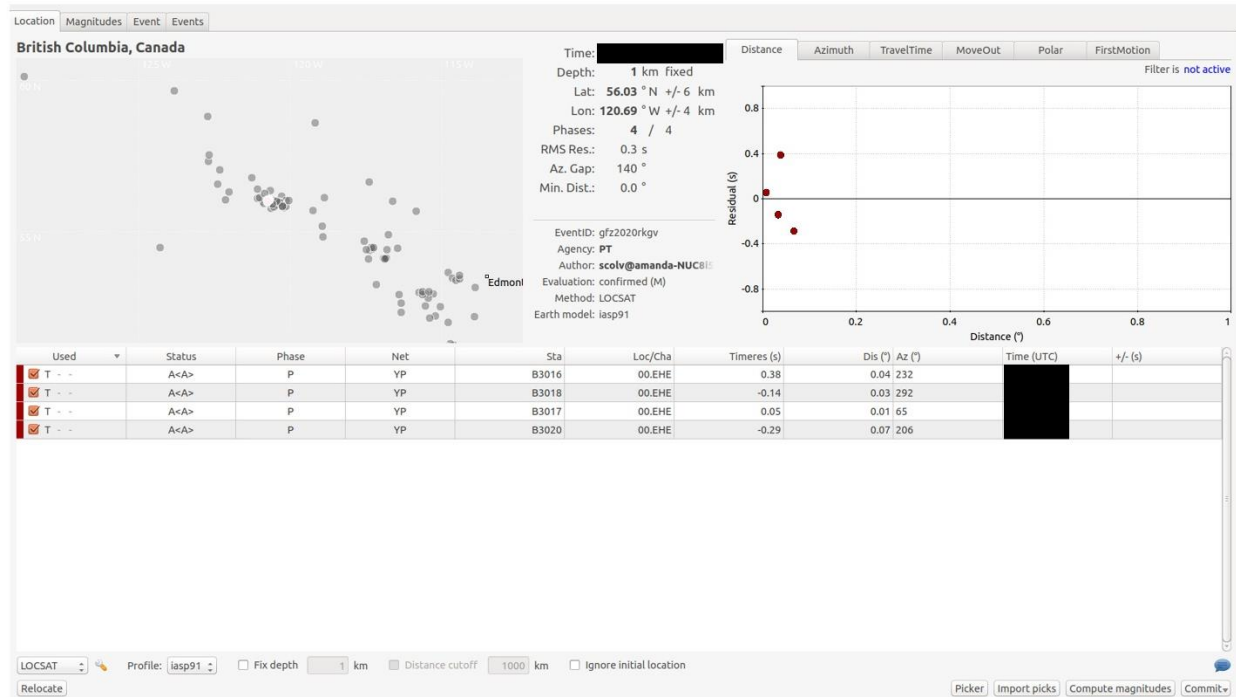


Figure 16. Screenshot from the scolv graphical user interface of SeisComP3 showing the picked arrivals, calculated location, and arrival residuals for event 252. Times are masked to conserve confidentiality.

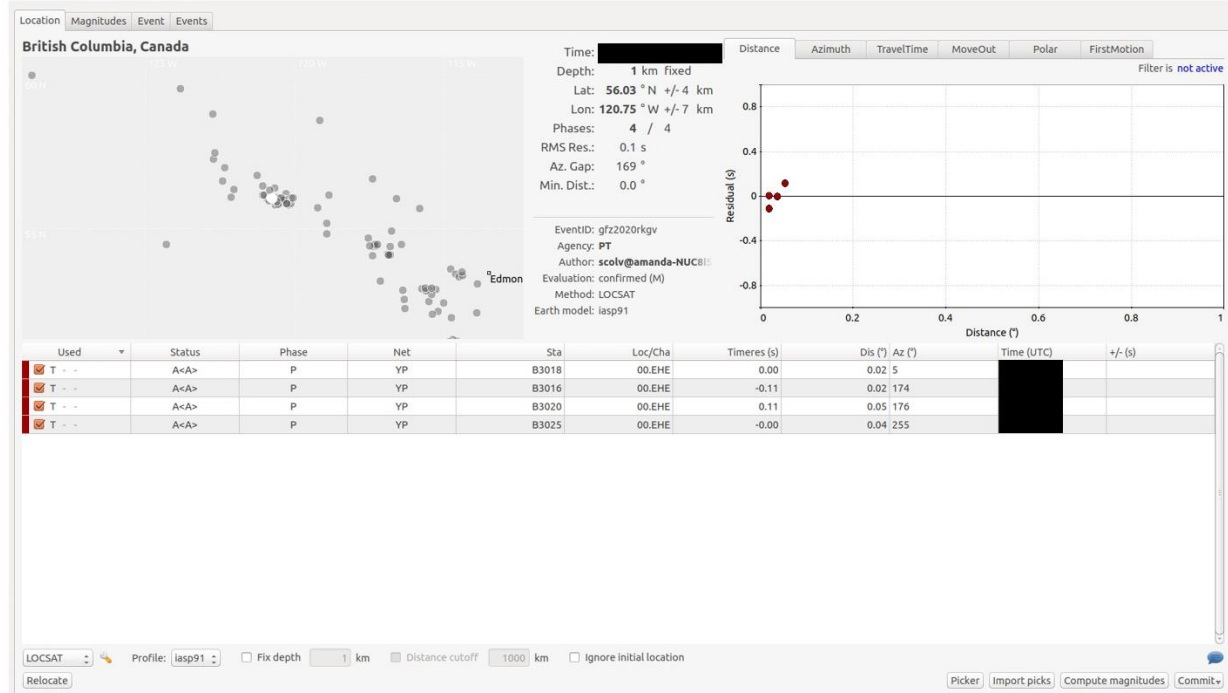


Figure 17. Screenshot from the scolv graphical user interface of SeisComP3 showing the picked arrivals, calculated location, and arrival residuals for event 253. Times are masked to conserve confidentiality.

The location of the regional broadband stations, with data available through IRIS, nearby our monitoring array, are shown, with respect to the stations in our array, in Figure 25. Given the proximity of several of the regional broadband stations to our array, their picks were combined with those from our geophones to obtain solutions for the anomalous induced events reported here. Figures 26-31 present an example of combining the datasets to determine a solution for event B, which was recorded by our accelerometers, and for which we have a final solution from the operator-deployed local broadband array. Figures 26 and 27 show the waveforms, picks, and resulting location for the event determined from our geophone data, while Figures 28 and 29 show the waveforms, picks, and resulting location from the regional broadband data. Table 4 compares the epicenters calculated from our geophone data and the regional broadband data with the solution reported from the operator-deployed local broadband array. The epicenter calculated from our geophone data is 106 m from the epicenter determined by the local broadband array, while the epicenter calculated from the regional broadband data is 108 m away. By combining picks from both datasets, we obtain a solution that is nearly identical to that from the local broadband array (<1m). The picks and resulting location for the combined datasets are shown in Figure 30. Figure 31 shows the local magnitude calculated for the event from the regional broadband stations, a value of 1.87, in comparison to the local broadband array reported moment magnitude of 1.98. A second

example showing the combined solution for event A is included in Figures 32 and 33; however, we do not have the reprocessed solution from the local broadband array for this event for comparison.

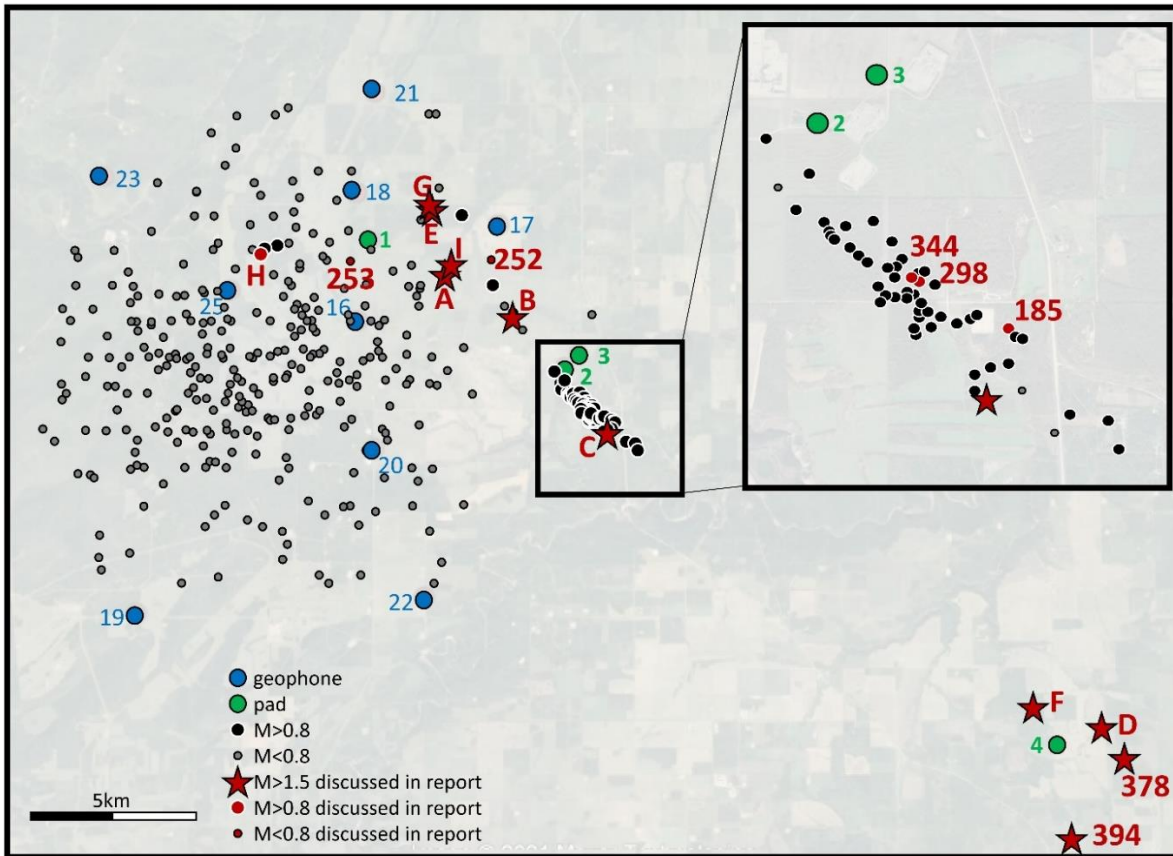


Figure 18. Map showing the earthquakes recorded during this study. Operationally-induced events with $M < 0.8$ are plotted as grey dots, except for events 251 and 252 discussed in this report, which are plotted as red dots. Anomalously-induced events with $M > 0.8$ are plotted as bigger black dots, except for events 185, 297, 343, and G, which are discussed in this report and plotted as bigger red dots. Anomalously-induced events with $M > 1.5$ that are discussed in this report are plotted as red stars. The pads are plotted as green dots and the geophones are plotted as blue dots. The inset box shows a zoomed in look at the events around pads 2 and 3. Geographic locations are not provided to conserve confidentiality.

The epicenters for the anomalous induced events, calculated by combining our geophone dataset with data from the regional broadband stations, are plotted in Figure 18 as black dots, while the events presented in this report with M 0.8–1.5 are plotted as red dots (events 185, 298 and 344) and those presented in this report with $M > 1.5$ are plotted as red stars (event A and B). The epicenters for the anomalous induced events with respect to pad 1 as well as local magnitudes when available are tabulated in Appendix 3. The vast majority of the anomalous induced events locate to the south of pads 2 and 3 apparently along a linear feature extending southeast from pad 2, along the same direction as mapped faults in the area (Fox et al. 2019 and references therein).

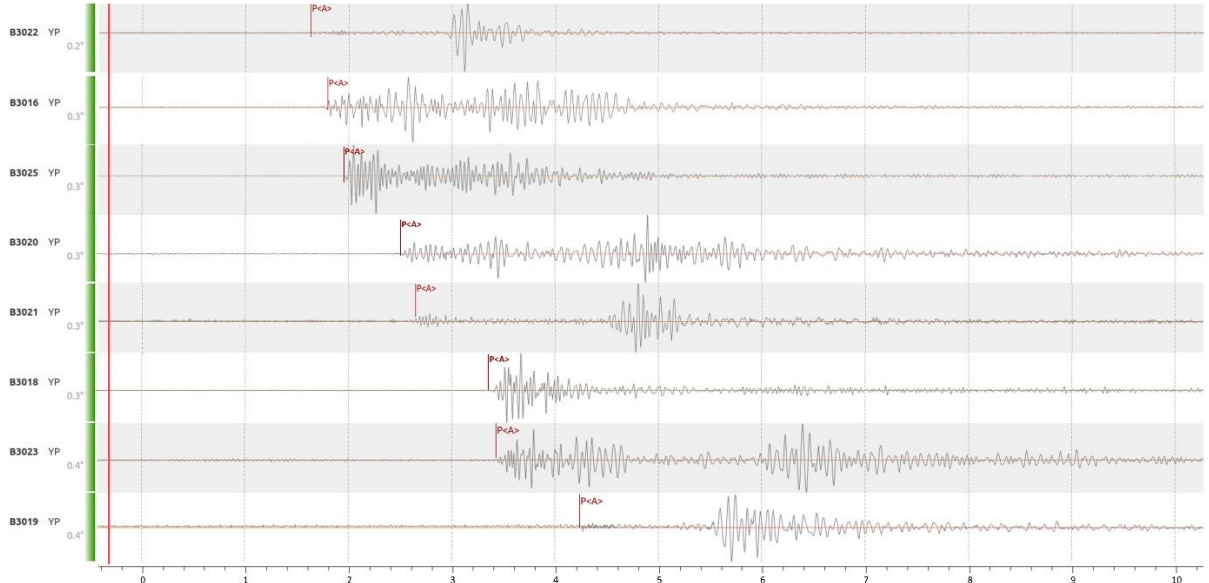


Figure 19. Waveforms for event 185 recorded on our geophones. The component shown for each station is indicated in Figure 20. Small red arrows, labeled P<A>, indicate the automatic picks made by our system. Large red line indicates the event time.



Figure 20. Screenshot from the scolv graphical user interface of SeisComP3 showing the picked arrivals, calculated location, and arrival residuals for event 185. Times are masked to conserve confidentiality.

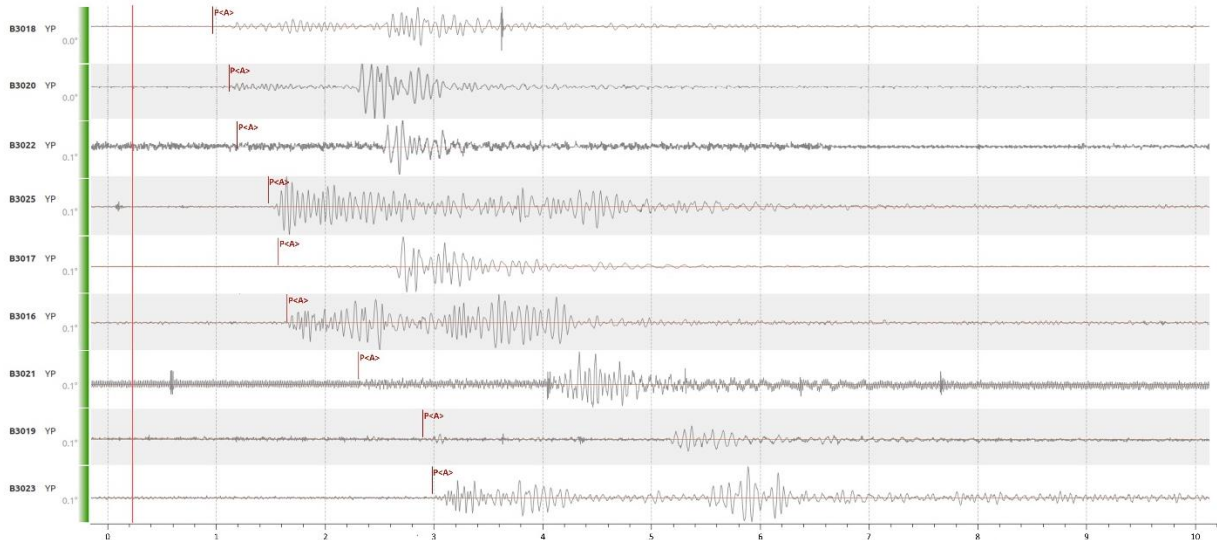


Figure 21. Waveforms for event 298 recorded on our geophones. The component shown for each station is indicated in Figure 22. Small red arrows, labeled P<A>, indicate the automatic picks made by our system. Large red line indicates the event time.

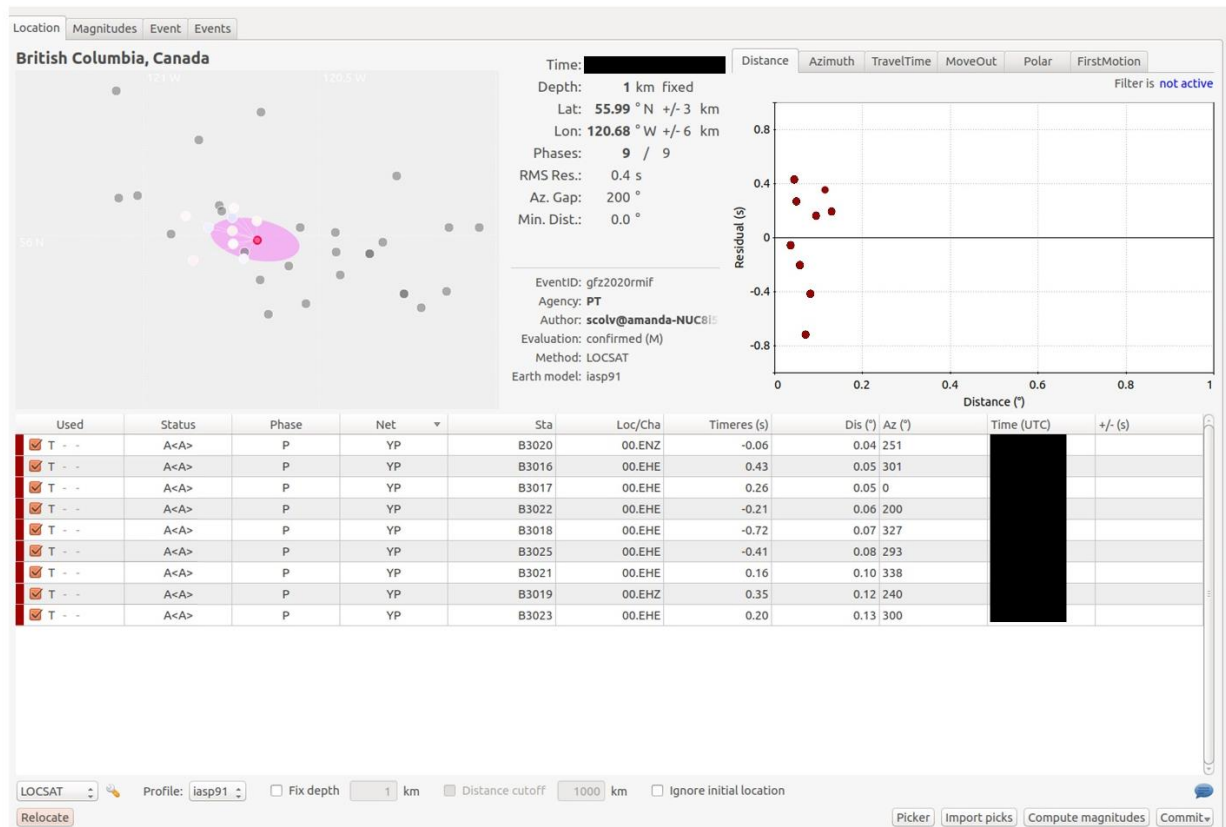


Figure 22. Screenshot from the scolv graphical user interface of SeisComP3 showing the picked arrivals, calculated location, and arrival residuals for event 298. Times are masked to conserve confidentiality.

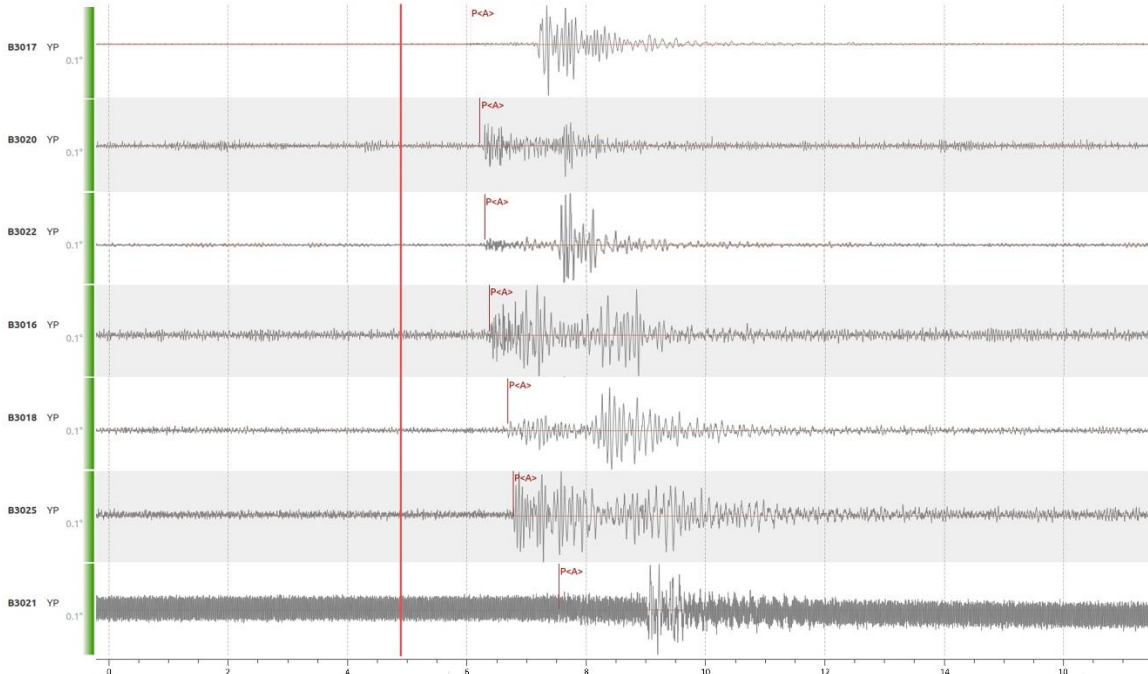


Figure 23. Waveforms for event 344 recorded on our geophones. The component shown for each station is indicated in Figure 24. Small red arrows, labeled P<A>, indicate the automatic picks made by our system. Large red line indicates the event time.

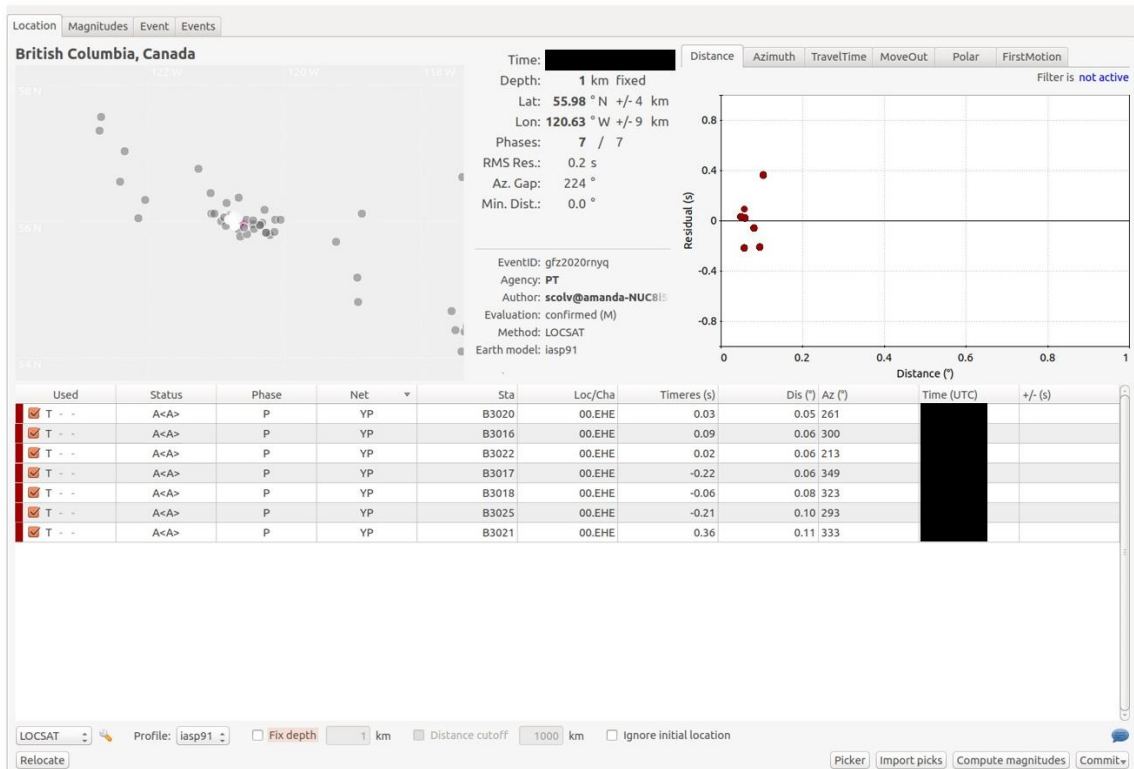


Figure 24. Screenshot from the scolv graphical user interface of SeisComP3 showing the picked arrivals, calculated location, and arrival residuals for event 344. Times are masked to conserve confidentiality.

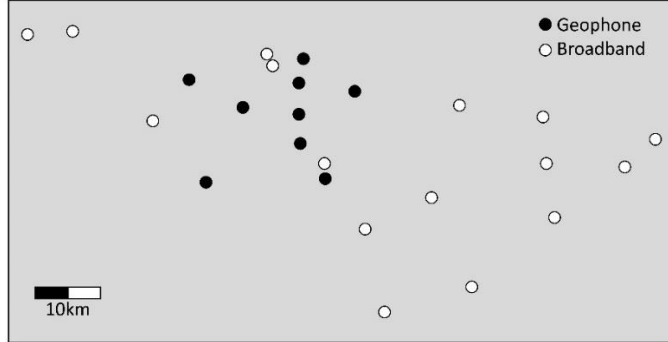


Figure 25. Location of the stations in our geophone array deployed for the dense monitoring (black dots) and the location of the regional broadband stations with data available through IRIS (white dots).

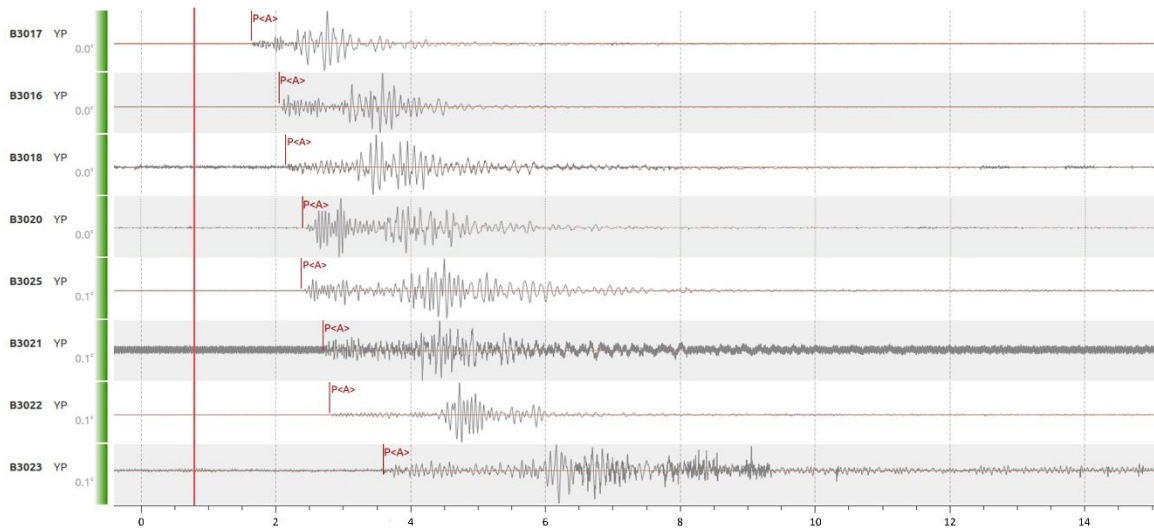


Figure 26. Waveforms for event B recorded on our geophones. The component shown for each station is indicated in Figure 26. Small red arrows, labeled P<A>, indicate the automatic picks made by our system. Large red line indicates the event time.

Our real-time automatic systems were only operational until the last day of pumping on pad 1; however, given the number of anomalous events that were induced post-injection (i.e., events C-I), we ran our system in offline mode to obtain solutions for the events detected by our accelerometers as well as to search for additional anomalous events. We searched for events within a 5-day period encompassing events C-G and calculated solutions for event H, which occurred another 5 days later, and event I, which occurred 23 days later. We locate 32 anomalous events induced within our monitoring areas during the 5-day period, in addition to the 5 events detected by our accelerometers (events C, E, G, H, and I). Table 4 shows a comparison of our epicenter for event E determined by combining our geophone data with the regional broadband data and the epicenter from the local broadband array. We obtain an epicenter 86 m from that of the regional broadband array and a local magnitude of 1.64 compared to the local broadband array reported moment magnitude of 1.67.

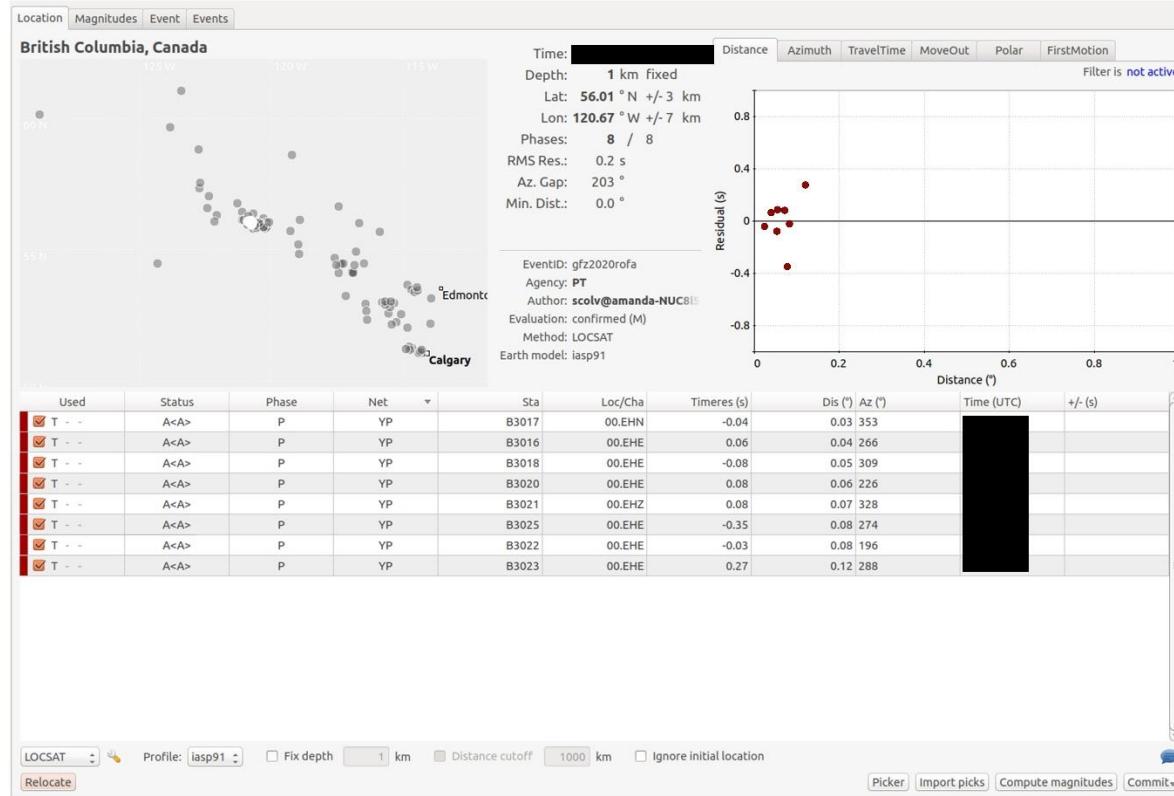


Figure 27. Screenshot from the scolv graphical user interface of SeisComP3 showing the picked arrivals, calculated location, and arrival residuals for event B recorded on our geophones. Times are masked to conserve confidentiality.

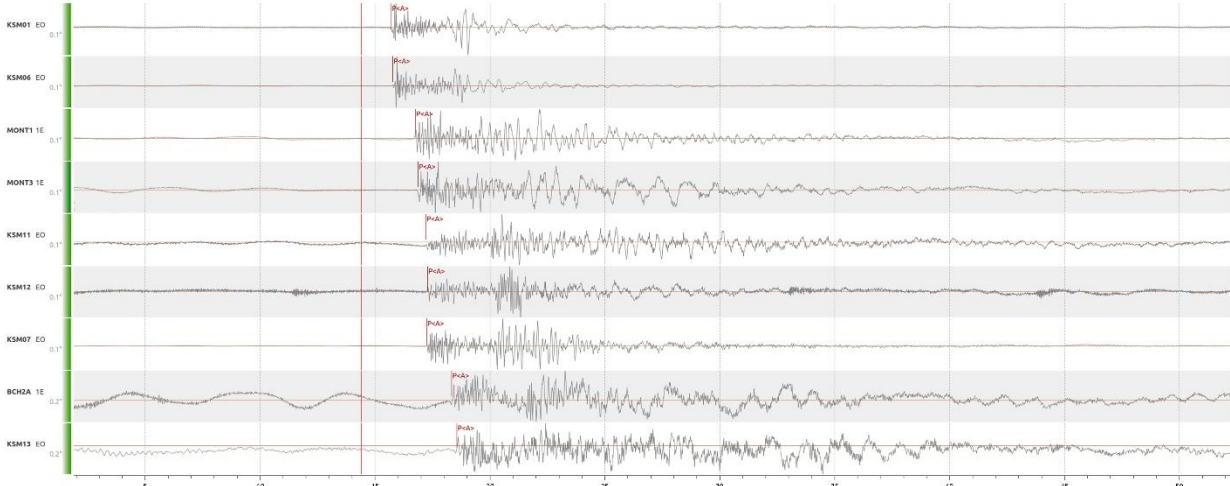


Figure 28. Waveforms for event B recorded on the regional broadband stations. The component shown for each station is indicated in Figure 29. Small red arrows, labeled P<A>, indicate the automatic picks made by our system. Large red line indicates the event time.

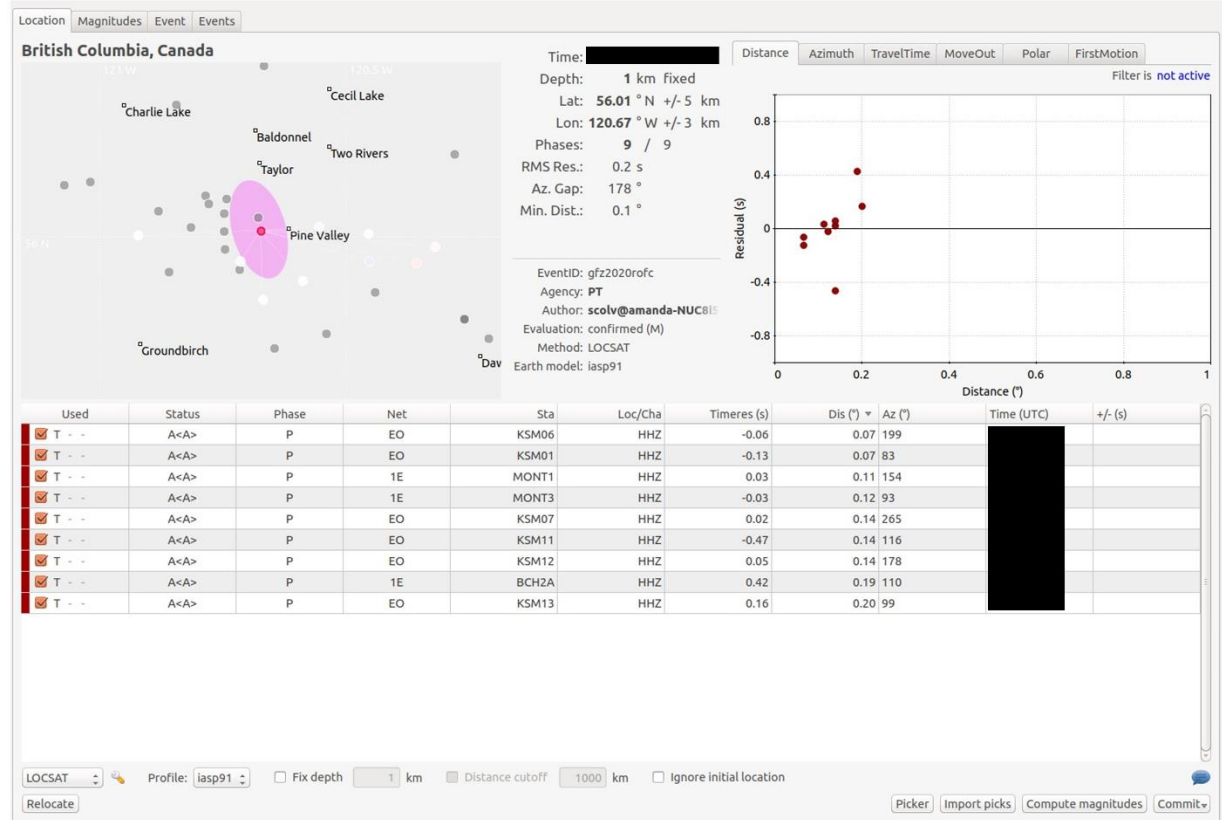


Figure 29. Screenshot from the scolv graphical user interface of SeisComP3 showing the picked arrivals, calculated location, and arrival residuals for event B recorded on the regional broadband stations. Times are masked to conserve confidentiality.

Table 4. The epicenter of event B calculated from our geophone data, the regional broadband data, and a combination of both datasets and the epicenter of event E from the combined datasets. The distance between the calculated epicenters and the epicenters reported from the operator deployed local broadband array (LBA) is also shown in meters.

	Event B			Event E
	Geophone	Regional BB	Combined	Combined
Latitude	56.01284	56.01282	56.01278	56.04156
Longitude	-120.67200	-120.67204	-120.67030	-120.71094
Distance from LBA (m)	106	108	0.778	85.8

The epicenters for the events located by our offline analysis are also plotted in Figure 18 and the epicenters and local magnitudes tabulated in Appendix 3. Two of the additional events locate near event H, while the other 30 events locate along the same linear feature extending southeast from pad 2. The inset plot in Figure 18 shows a zoomed in view of the epicenters and how they appear to delineate a fault. While event C also plots along this linear feature, events A, B, E, G, I, the largest of the events induced near pad 1, all plot further northeast. These five $M > 1.5$ events induced closer to pad 1 than pads 2 and 3

also appear to locate along the same southeast-northwest oriented linear feature as the events to the south of pads 2 and 3. While our coverage is poor in this area, we are confident we have not missed any events with magnitudes greater than around 0.7. The linear feature delineated by the anomalous events south of pads 2 and 3 is approximately 3.5 km in length. If such a fault exists, it is important to understand why it only induced events with $M < 2.5$ and the entire fault did not rupture in a larger event (ex. $M \sim 4$). If the events with $M > 1.5$ located closer to pad 1 are along the same fault plane as the events south of pads 2 and 3, then this question becomes more critical. We theorize that the non-critical orientation of the fault (approximately perpendicular to the maximum horizontal stress), possibly combined with the abnormally high pore pressure resulting from three nearby (in time and space) operations allowed the fault to mostly fail aseismically (discussed further in the Hydro-Geomechanical Modelling section). Understanding how a 10 km long fault would react to hydraulic fracturing operations occurring at either end will be investigated in future 3-D hydro-geomechanical modelling work.

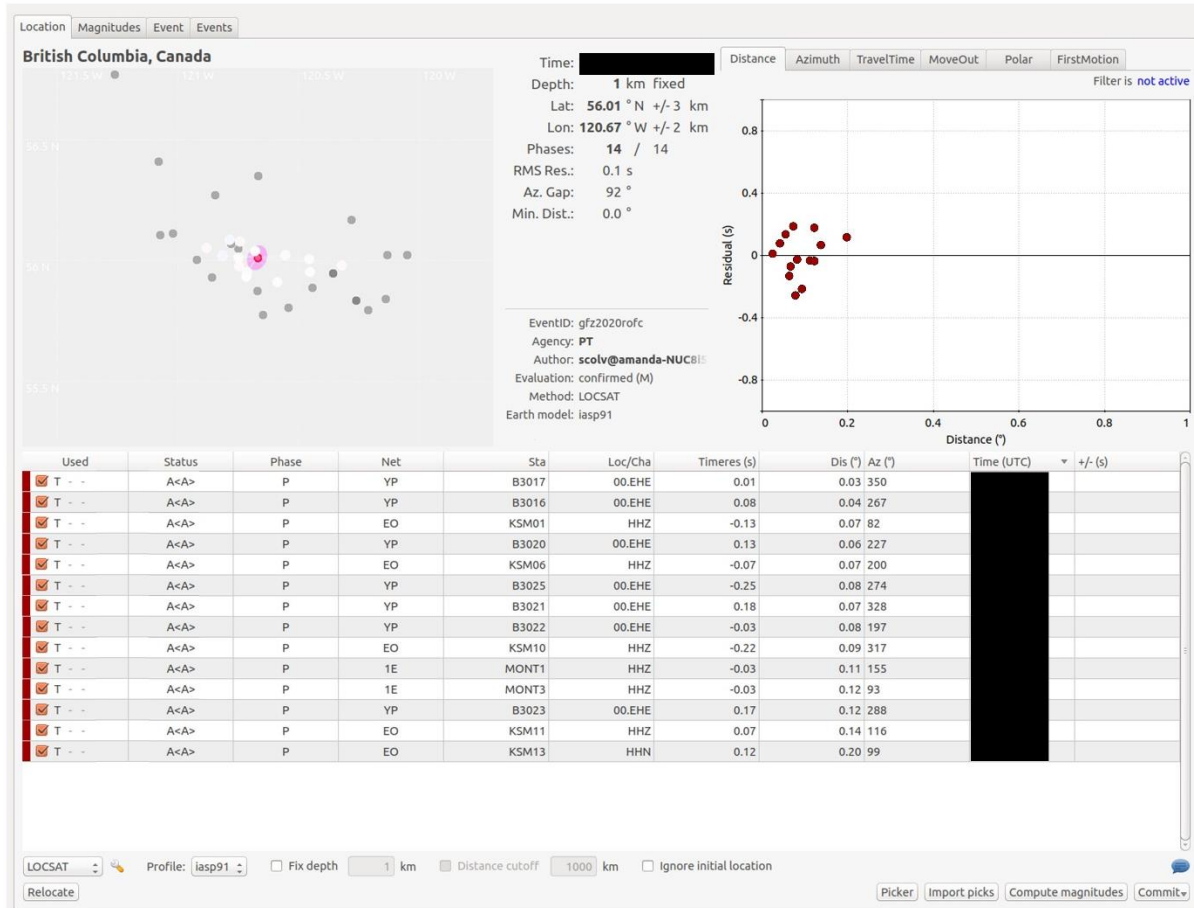


Figure 30. Screenshot from the scolv graphical user interface of SeisComp3 showing the picked arrivals, calculated location, and arrival residuals for event B recorded on a combination of our geophones and the regional broadband stations. Times are masked to conserve confidentiality.

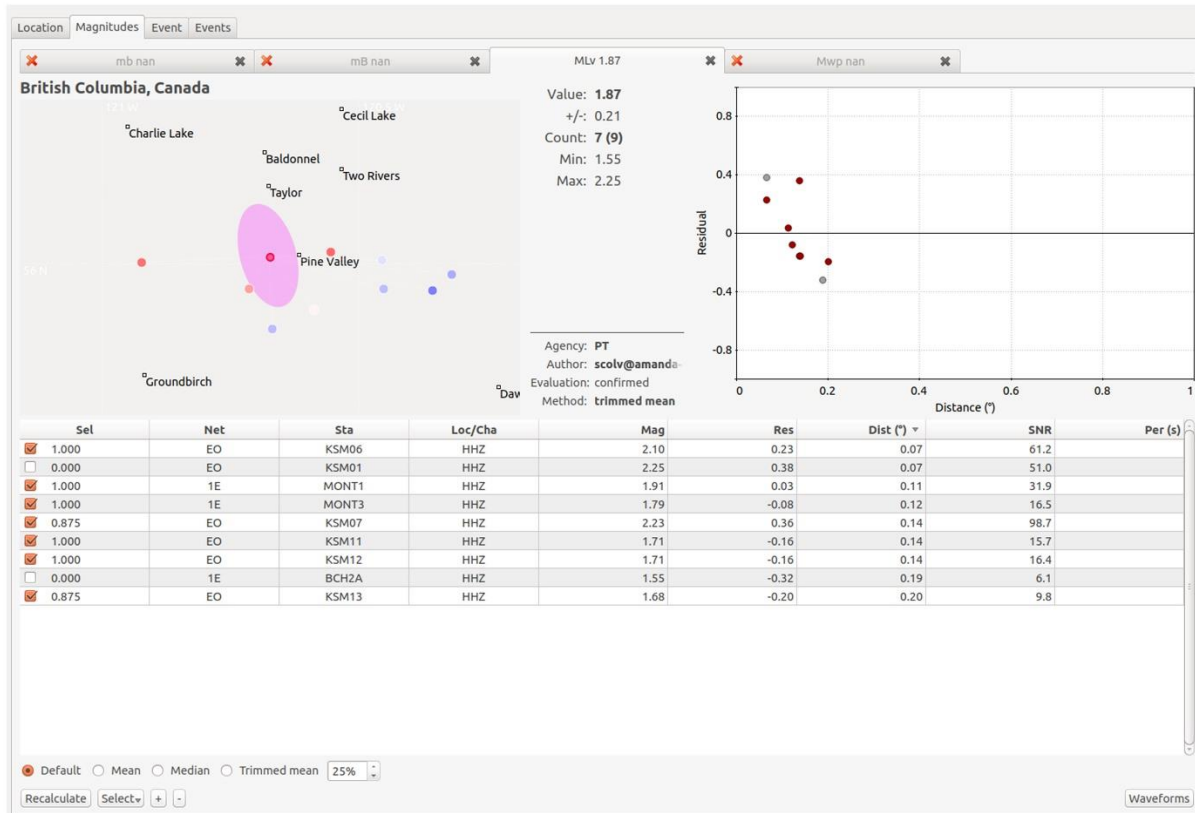


Figure 31. Screenshot from the scolv graphical user interface of SeisComP3 showing the calculated local magnitude for event B recorded on the regional broadband stations.

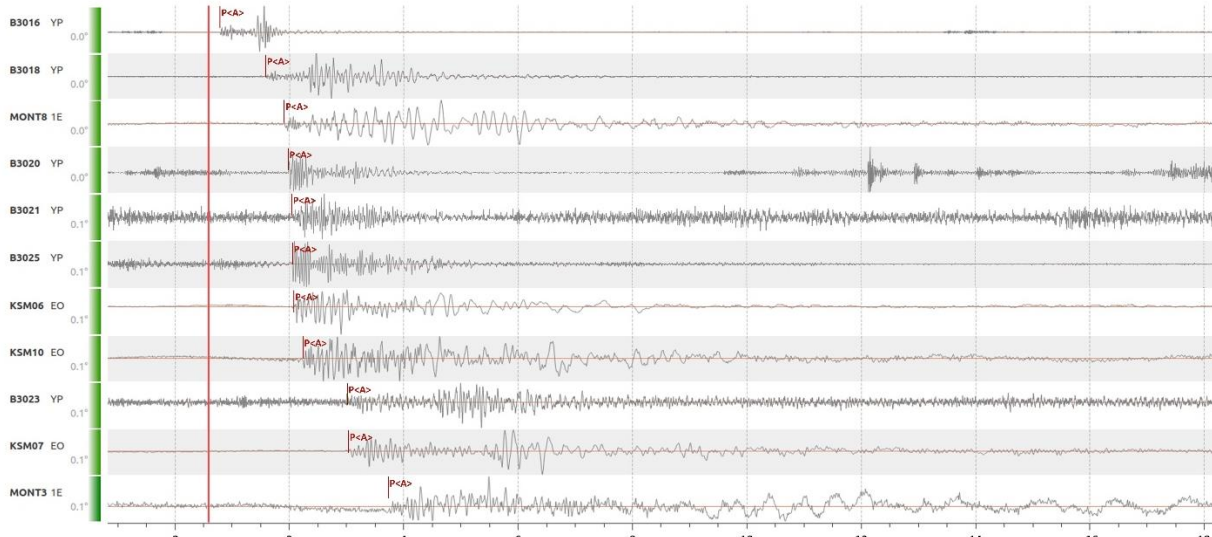


Figure 32. Waveforms for event A recorded on our geophones and the regional broadband stations. The component shown for each station is indicated in Figure 32. Small red arrows, labeled P<A>, indicate the automatic picks made by our system. Large red line indicates the event time.

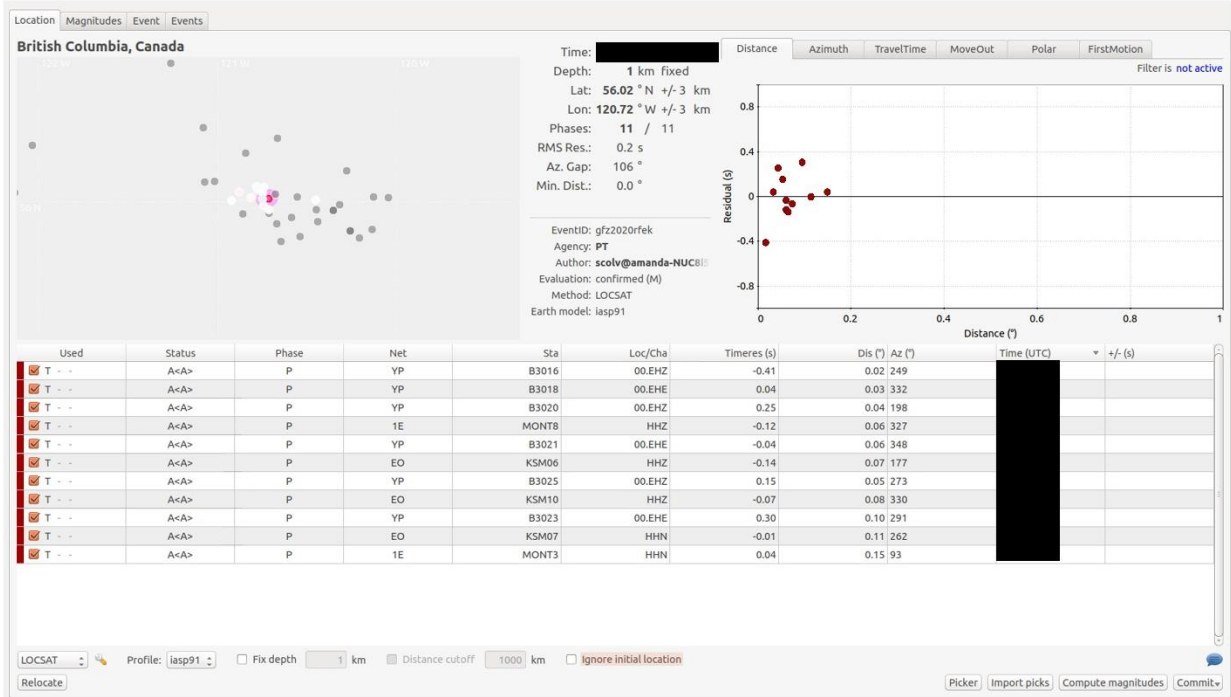


Figure 33. Screenshot from the scolv graphical user interface of SeisComP3 showing the calculated local magnitude for event A recorded on a combination of our geophones and the regional broadband stations.

In addition to the events detected during the 5-day period of offline processing, which were located near our monitoring area, we locate 154 anomalous events induced near pad 4 as well as events D and F detected by our accelerometers. Given the distance of our array to pad 4, these events were mainly located with the regional broadband stations. An example is presented in Figures 34-36, which show the waveforms, picks, and calculated location and magnitude for event F, the largest event recorded during the four hydraulic fracturing operations. Event F and event D were both reported by NRCan, as were two other events near pad 4 (events 378 and 394). A comparison between the epicenters and local magnitudes calculated from our system with those reported by NRCan are presented in Table 5. To the accuracy provided by NRCan, our epicenters vary from 0 to 780 m from the NRCan solutions and three of our solutions provide the same magnitude and one is 0.1 local magnitude units higher. As most of the anomalous induced events near pad 4 were not located using our geophones and the same care was not given to confirming picks, we have not plotted the 154 events. We note; however, that unlike the anomalous events detected south of pads 2 and 3, the events near pad 4 are elongated along the direction of the maximum horizontal stress, suggesting a more critically oriented fault, which would release more seismic energy, possibly explaining why pad 4 induced a higher frequency of anomalous induced events with larger magnitudes.

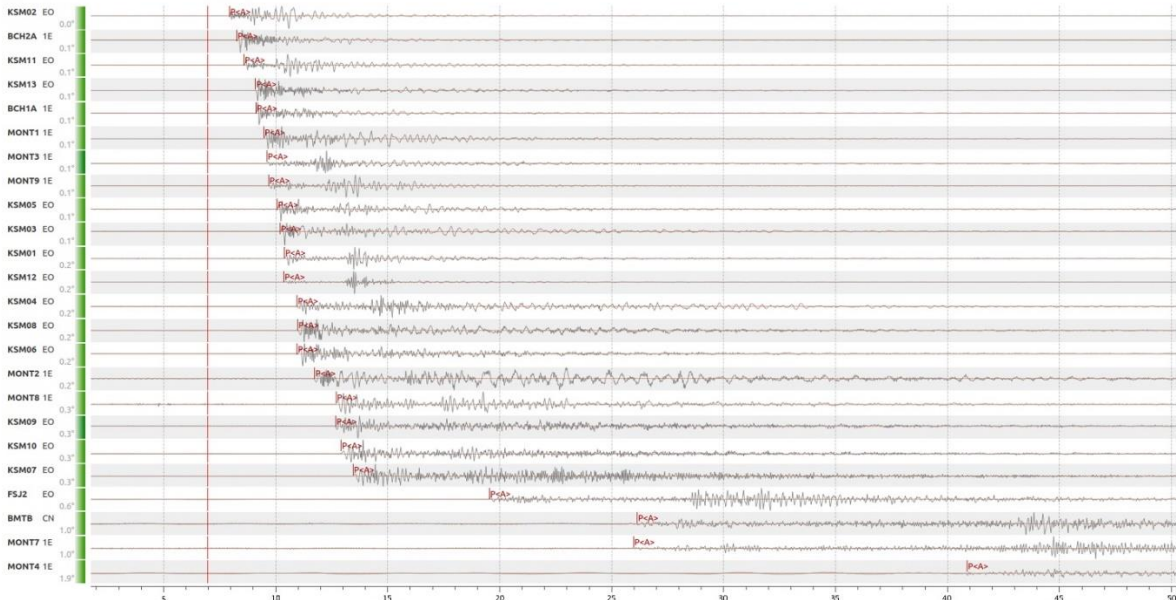


Figure 34. Waveforms for event F recorded on the regional broadband stations. The component shown for each station is indicated in Figure 35. Small red arrows, labeled P<A>, indicate the automatic picks made by our system. Large red line indicates the event time.

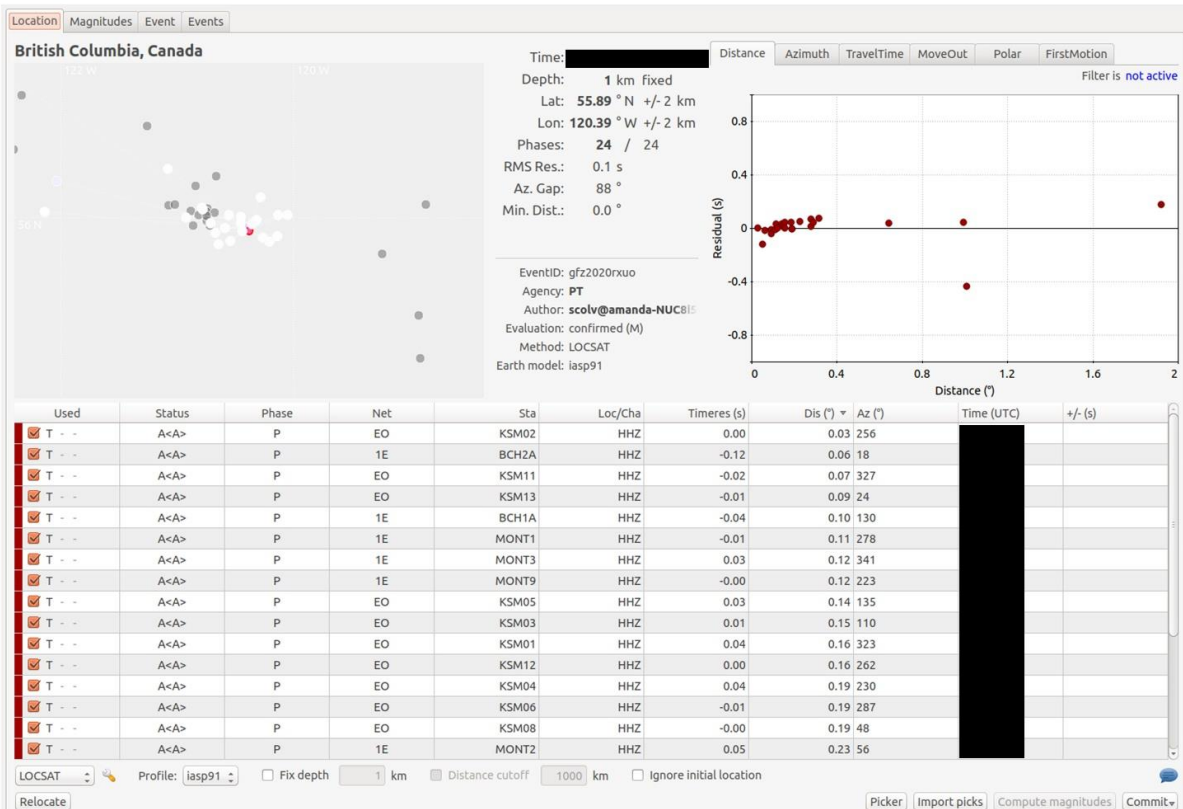


Figure 35. Screenshot from the scolv graphical user interface of SeisComP3 showing the picked arrivals, calculated location, and arrival residuals for event F recorded on a combination of our geophones and the regional broadband stations. Times are masked to conserve confidentiality.

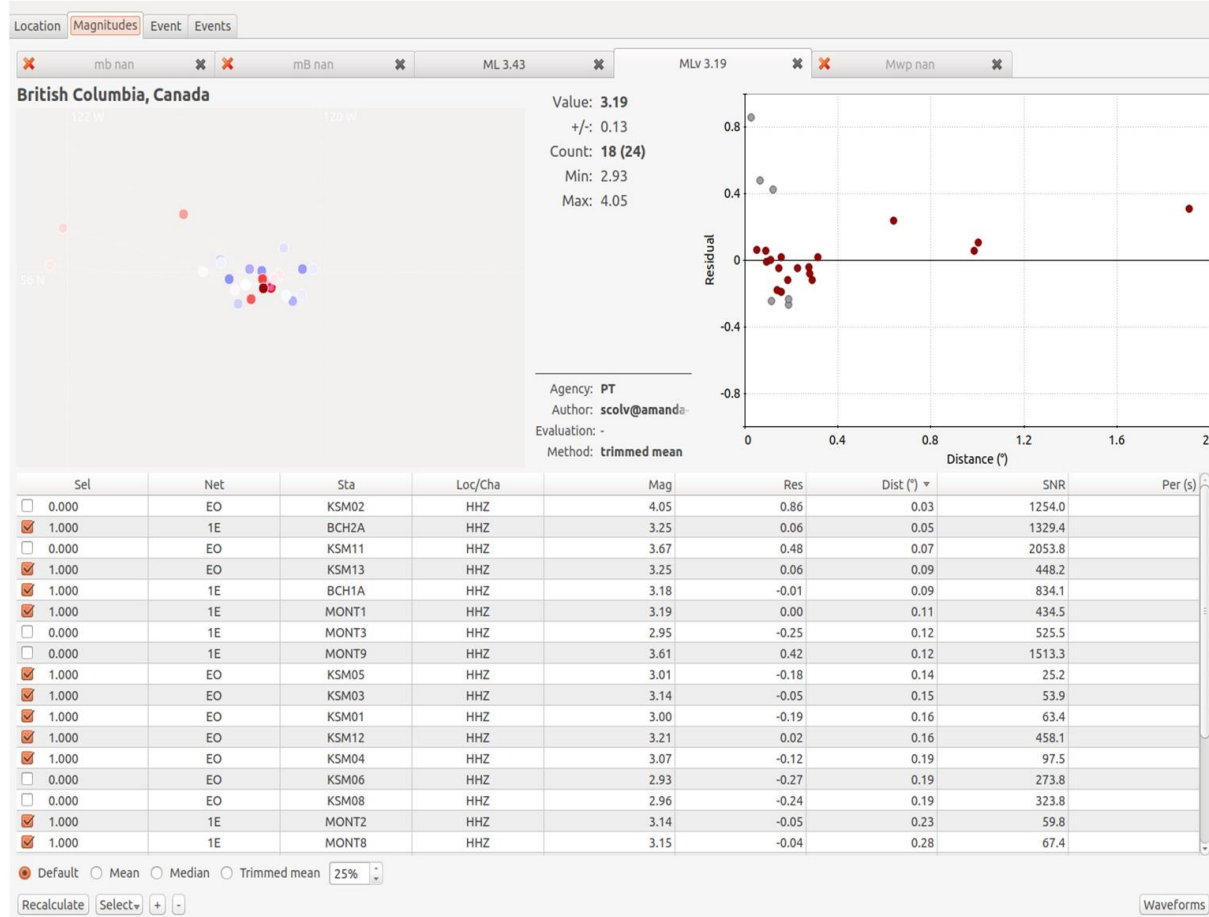


Figure 36. Screenshot from the scolv graphical user interface of SeisComP3 showing the calculated local magnitude for event F recorded on the regional broadband stations.

Table 5. Comparison of solutions obtained in this study with solutions reported by NRCan.

Event ID	Our Solutions			NRCan Solutions			Difference in Epicenter	Difference in M_L
	Latitude	Longitude	M_L	Latitude	Longitude	M_L		
C	55.896	120.377	2.5	55.898	120.375	2.5	255 m	0
392	55.866	120.393	2.2	55.866	120.393	2.2	0	0
E	55.895	120.391	3.2	55.896	120.396	3.2	331 m	0
376	55.887	120.365	2.4	55.894	120.366	2.3	781 m	0.1

Hydro-Geomechanical Modelling

The main objective of this project was to design and build a monitoring array capable of providing data for researchers not available through regional or small local broadband arrays, while also providing a cost-effective alternative for industry to meet their monitoring requirements, even in areas with low magnitude thresholds. A second objective was to integrate data recorded by our array into 3D hydro-

geomechanical models to investigate the impact of mitigation strategies and better understand the processes and parameters controlling anomalous induced events. In particular, physics-based 3D modelling with accurate hydro-geomechanical parameters is required to understand what fluid injection operations will induce seismicity, which faults will be susceptible to unstable slip, what is the maximum magnitude for induced seismicity, and what mitigation strategies will be the most effective for reducing the hazard of induced seismicity.

Early models conceptualized induced seismicity as resulting from seismic slip on faults directly induced by the diffusion of increased pore pressures from fluid injection. The pore pressure diffusion model for induced seismicity predicts the magnitude of anomalous events to increase with time and as such traffic light protocols would be effective at mitigating hazardous events. Most of the operations we monitored induced events which followed similar patterns as anticipated from the pore pressure diffusion model. However, the largest event we recorded, the only $M>4$ induced by hydraulic fracturing to date in the KSMMA (event #3 of operation #6) was not preceded by any yellow-light events ($M>2$) and occurred early in the sequence of events (#3 of 18 $M>1.5$ events). The largest event recorded in the Montney, a M_w 4.6 on August 17th, 2015, was also not preceded by yellow-light events. Therefore, the most hazardous events induced in the Montney did not follow the anticipated pore pressure diffusion model and could not have been mitigated by traffic light protocols. Additionally, some of the data from the operations we monitored do not follow the anticipated relationship between maximum magnitude and numbers of events. Operation #6, which induced the $M>4$ event, our largest recorded event, induced a total of 18 $M>1.5$ events, while operation #7 induced 26 $M>1.5$ events with a maximum magnitude of 2.4 and we detected 56 $M>1.5$ events with a maximum magnitude of 3.2 for the operation on pad 4, which we unintentionally monitored during our dense array monitoring. A better understanding of the processes controlling the magnitude and frequency of anomalous events induced by hydraulic fracturing operations is needed before better mitigation and prevention frameworks can be developed.

Evidence from recent research suggests that with increasing fluid pressures, fault friction mainly becomes rate strengthening, which favors stable aseismic slip and not dynamic failure needed for earthquakes (Scuderi et al., 2018; Cappa et al., 2018; 2019). A different conceptual model where fluid injection induces aseismic slip on a fault, which then triggers seismic slip has thus been suggested by many authors (Bhattacharya and Viesca, 2020; Eyre et al., 2019; Guglielmi et al., 2020; Wynants-Morel et al., 2020). We test this conceptual model by comparing the resulting slip on a fault from fluid injection through hydraulic fractures for different values of fault residual friction and compare the results to the variations in fault behaviours we observed during our monitoring operations. We compare the results from three simulations; 1) lower residual than initial friction; 2) higher residual than initial friction; and 3)

higher residual than initial friction on the portion of the fault containing the hydraulic fracture planes and lower residual than initial friction on the rest of the fault. The first model reproduces a friction weakening fault favoring seismic slip, the second a friction strengthening fault favoring aseismic slip, and we test with the third model whether seismic slip is triggered by aseismic slip on the fault. For the modelling, we use 3DEC™ (versions 5.2 and 7.0), a discontinuum-modelling code based on distinct-element method (DEM) software developed by Itasca Consulting Group Inc. (2020).

We start with a model similar to that developed for the Horn River Basin by Yin et al. (2020), except we adopt the principal stress magnitudes from Fox et al. (2019) derived for the Montney. Our model geometry is 1300 m in length in the direction of the maximum horizontal stress, 600 m wide, and 800 m in height. The middle of the model is set to a depth of 2400 m. A cluster of 5 hydraulic fracture planes, 500 m long and 100 m high, spaced 15 m apart, and oriented in the direction of the maximum horizontal stress, are added to the centre of the model, with injection at a rate of 0.17 m³/s in the middle of each plane. The fault is vertical, 425 m long, 400 m high, oriented at 45° and is centered 50 m from the middle of the model (and the injection points) in the direction of the hydraulic fracture planes (i.e., along the length axis of the model). If the entire fault failed seismically, a maximum magnitude ~4.5 event would be expected. Following the results of Fox et al. (2019), we apply a strike-slip stress regime to our model with a maximum horizontal stress gradient of 35 kPa/m, minimum horizontal stress gradient of 22 kPa/m, vertical stress gradient of 25 kPa/m, and an initial pore pressure gradient of 14 kPa/m.

The static friction angle for the fault is set at 30° for the three models. In model 1, a residual friction value of 22° was used and a value of 40° was used for model 2. For model 3, the middle portion of the fault, 100 m high and 500 m long, containing the hydraulic fractures was given a residual friction value of 40°, while the rest of the fault had a value of 22°. We first simulate fully-coupled hydrogeomechanical models with the deformation controlled by the basic Mohr-Coulomb slip criterion. The nonlinear softening-healing Coulomb slip constitutive model, newly implemented in the newest version of 3DEC (7.0), which allows the friction to return to its initial value after slipping stops and allows the shear strength to gradually decrease from its initial values, was then tested. A plot showing the model geometry is included in Figure 37 and the model parameters we used are tabulated in Table 6.

To compare the results from the three models using the Mohr-Coulomb slip criterion, we track the amount of shear slip that occurs on each segment of the fault (i.e., each sub-contact) every 2 minutes for 28 minutes of injection. We also track the normal stress and velocity of the shear displacement at each sub-contact. We then calculate the moment of energy released at each sub-contact by multiplying the slip by the sub-contact area and the shear modulus of the rock matrix. If the slip occurred at velocities greater than 0.5 mm/s and with normal stress on the fault segment greater than 5 MPa, we store the

moment as seismic moment, otherwise we store it as aseismic moment. Every 2 minutes, the seismic and aseismic moments are summed, and we compare the cumulative seismic, aseismic, and total moment for 28 minutes of injection for the three models. The calculated moments at each step for the three models are plotted versus injection time in Figure 38 and the calculated cumulative moments are plotted in Figure 39. The magnitude of the shear slip along the fault for the three models after 2, 14, and 28 minutes of injection is shown in Figures 40-42.

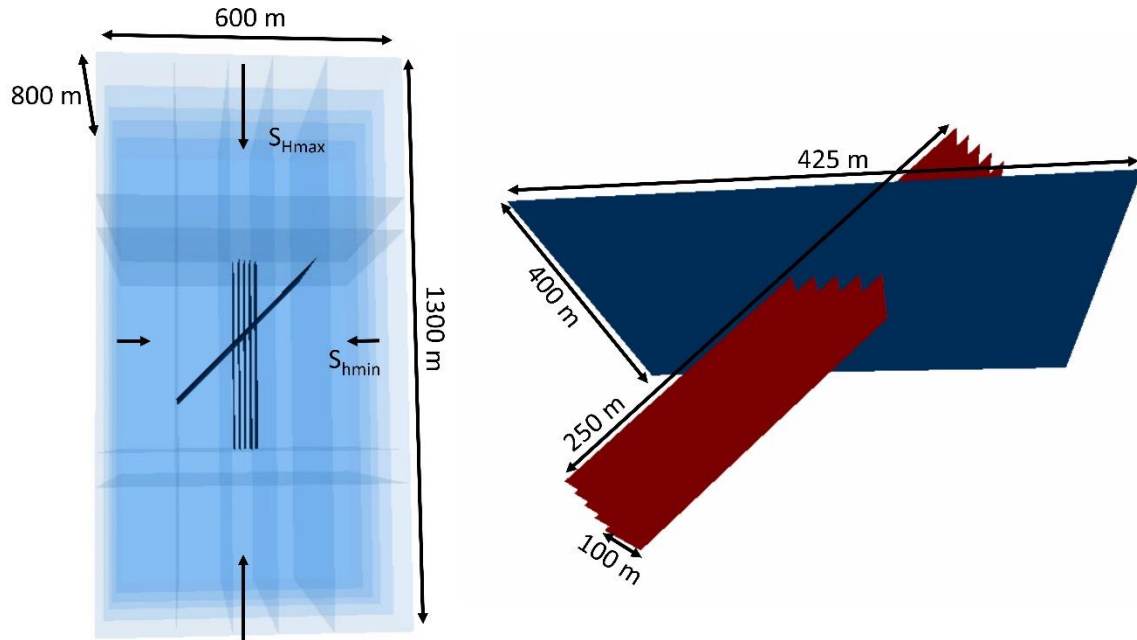


Figure 37. The geometry of our 3DEC models. (Left) Top view of our model showing the 5 parallel hydraulic fracture planes with the cross-cutting fault plane and their orientations with respect to the principal horizontal stress. (Right) 3D view of the fault (blue) plane and the 5 hydraulic fracture planes (red) and their geometries.

Table 6. Input parameters for our 3DEC models.

Block material			Fluid material					
Density (kg/m ³)	Young's modulus (GPa)	Poisson's ratio	Density (kg/m ³)	Viscosity (Pa s)	Injection rate (m ³ /s)			
2550	50	0.22	1200	0.02	0.17			
Joint material	Initial aperture (mm)	Normal stiffness (GPa/m)	Shear stiffness (GPa/m)	Friction angle (°)	Residual friction angle (°)	Dilation angle (°)	Cohesion (MPa)	Tensile strength (MPa)
HF	0.05	100	50	40	0	7.5	50	0
Fault	0.2	20	10	30	22/40	7.5	0	0

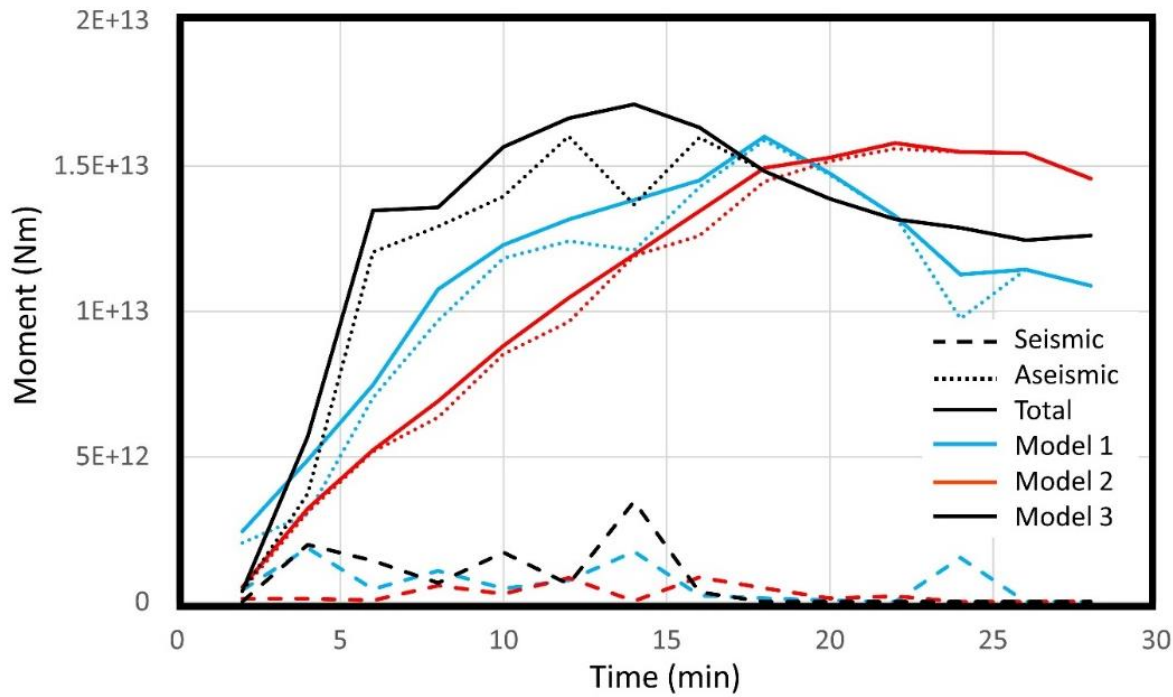


Figure 38. Graph of the seismic (dashed), aseismic (dotted), and total (solid) moment released every 2 minutes by model 1 (weakening, blue), model 2 (strengthening, red), and model 3 (partitioned, black).

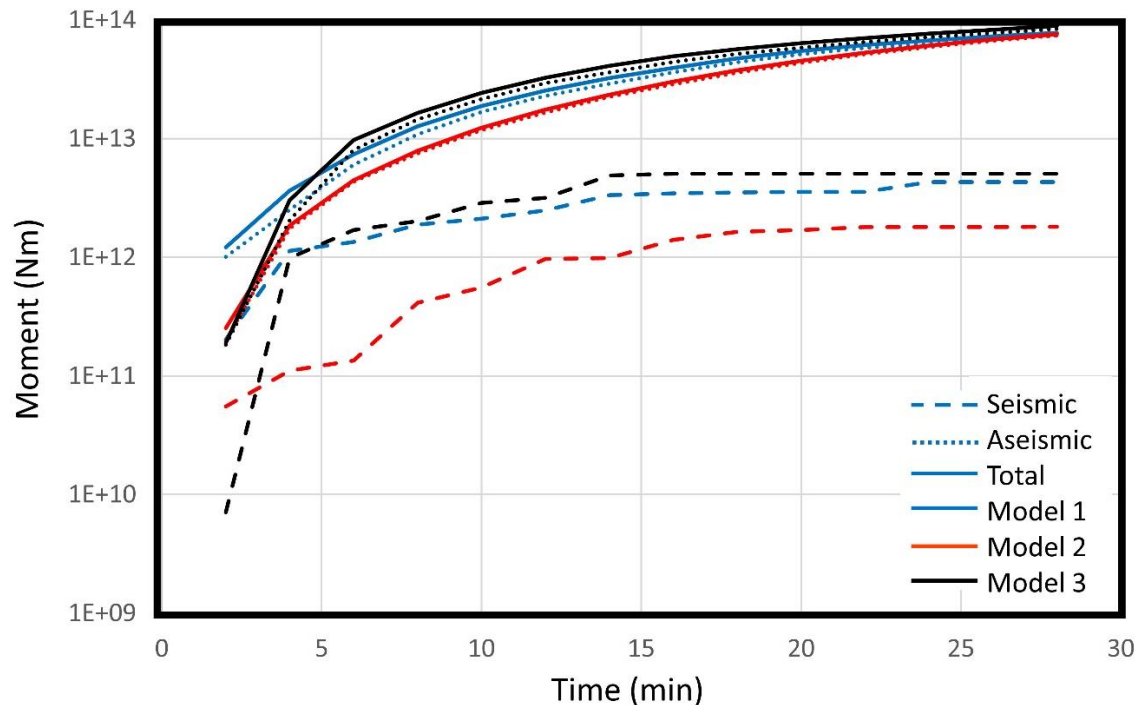


Figure 39. Graph of the cumulative seismic (dashed), aseismic (dotted), and total (solid) moment released by model 1 (weakening, blue), model 2 (strengthening, red), and model 3 (partitioned, black).

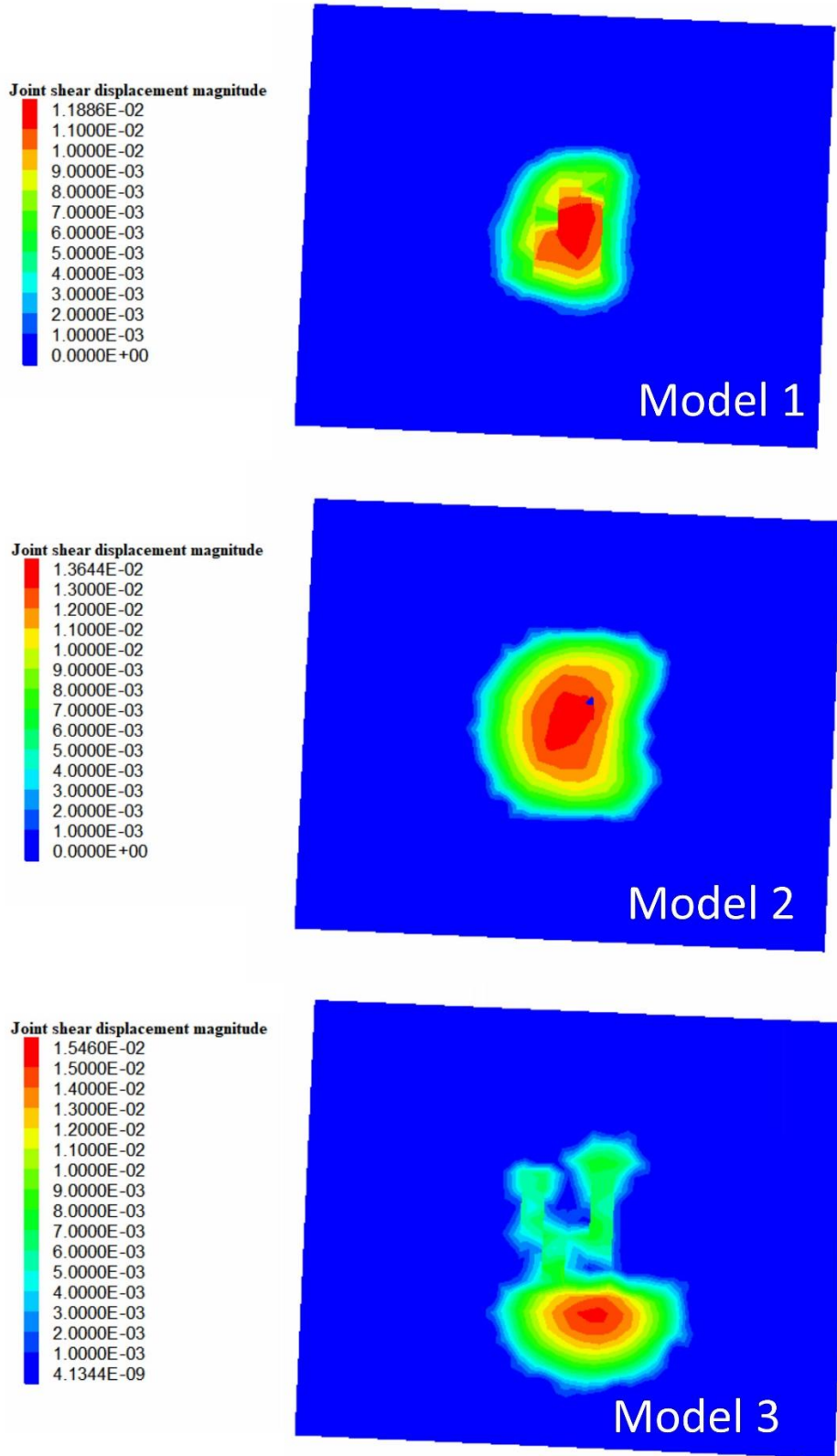


Figure 40. Shear displacement on the fault plane predicted from our three models after 2 minutes of injection (cross-sectional view).

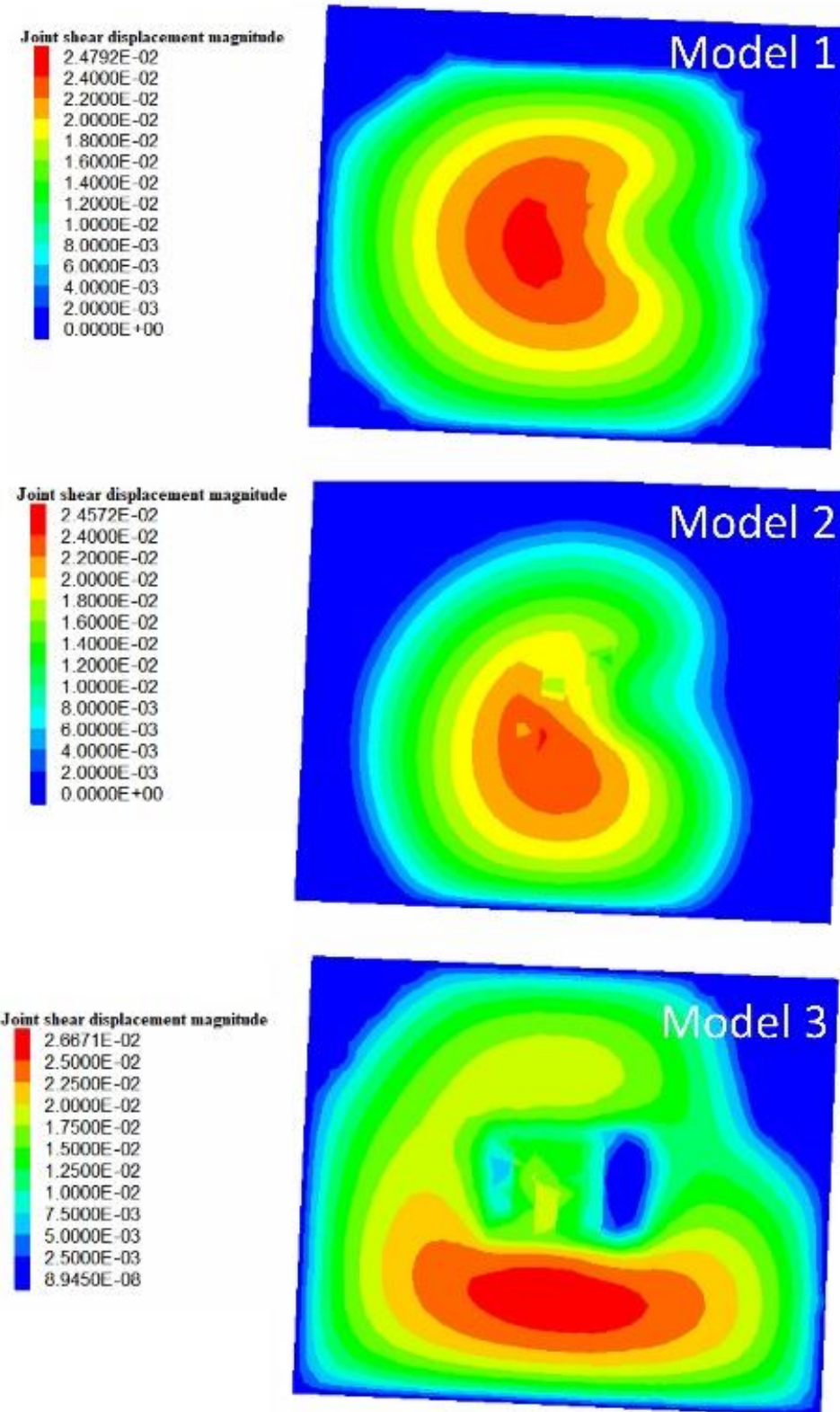


Figure 41. Shear displacement on the fault plane predicted from our three models after 14 minutes of injection (cross-sectional view).

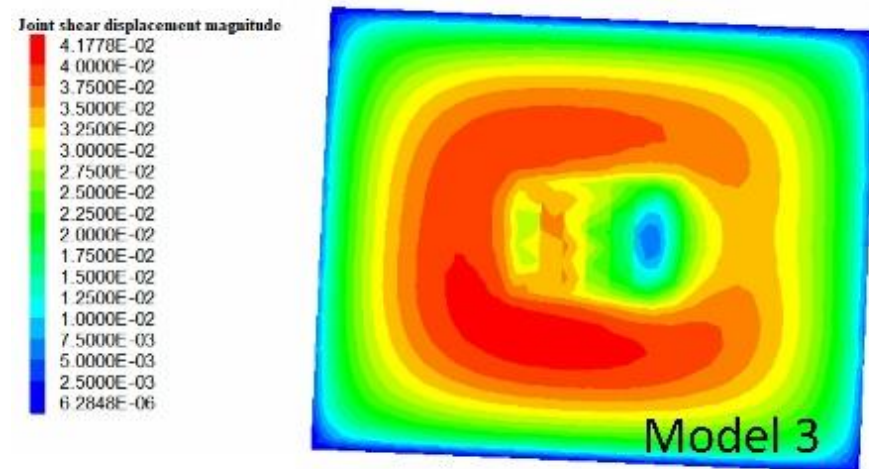
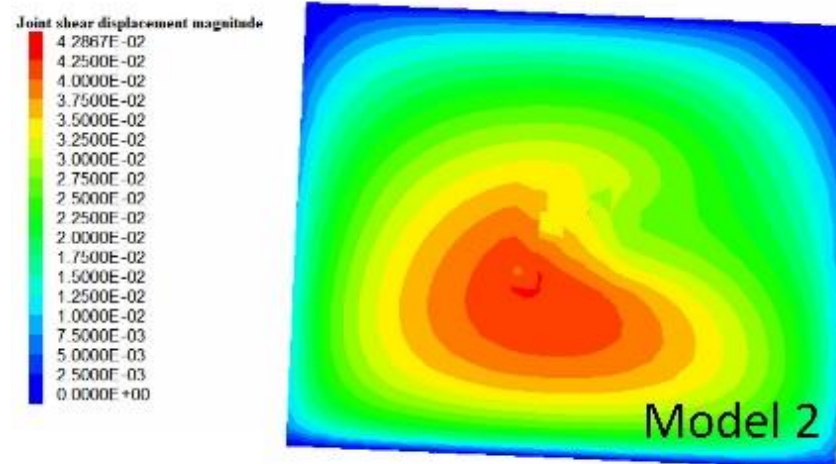
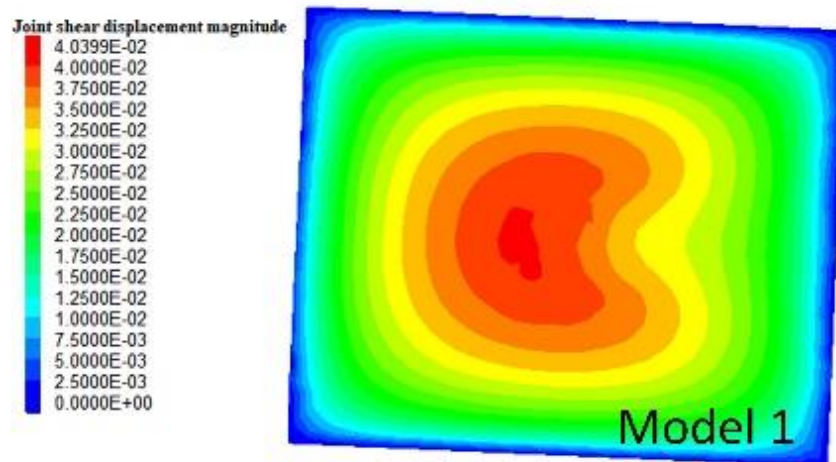


Figure 42. Shear displacement on the fault plane predicted from our three models after 28 minutes of injection (cross-sectional view).

The results from all three models predict almost full fault failure after 28 minutes of injection. Model 1, with weakening, predicts only 3% higher moment released than model 2 with strengthening. The moment released by model 3, with the partitioned residual friction, is 7% higher than the model 1 with weakening and 10% higher than the model 2 with strengthening. If the total moment was released seismically, model 3 would predict a M_w 4.06 event, model 1 would predict a M_w 4.01 event, and model 3 would predict a M_w 3.96 event. While all three model predict significantly higher aseismic than seismic moment, the ratio between seismic to aseismic moment is quite different. Model 1 predicts a minimum ratio of seismic to aseismic moment of 2.23 after 4 minutes and a maximum of 17.2 after 28 minutes. In comparison, model 2 predicts a maximum ratio of 41.1 after 28 minutes of injection. Model 3 initially has a high ratio of aseismic to seismic moment (26 after 2 minutes), which quickly decreases to 2.07 after 2 minutes of injection and increases to a maximum of 16.8 after 28 minutes.

The cumulative aseismic moment released, for all three models, increases more steadily compared to the cumulative seismic moment, which increases in steps until a point where it remains constant. All of the seismic moment is released by 24 minutes of injection for model 1, whereas model 3 has released all of the seismic moment by 14 minutes of injection. While the cumulative seismic moment released by model 1 and model 3 are similar after 28 minutes of injection, the timing for the release is different as evident from Figure 38. The most obvious difference between the two models is between the cumulative seismic moments from the start until 4 minutes. Significant seismic moment is released by model 1 during the first 2 minutes of the simulation compared to model 3, which mainly slips aseismically. After 2 minutes of injection, model 1 predicts 29 times higher seismic moment released than model 3, but only 1.1 times more after 4 minutes of injection.

These results suggest that for a strength weakening fault, the seismic moment is released steadily as a number of smaller events, such as predicted by the pore pressure diffusion model. In comparison, a fault that initially fails aseismically more quickly releases the same amount of energy as fewer, larger events. To test whether a fault that initially fails aseismically predicts fewer, larger events than the pore pressure diffusion model, we developed a script to spatially cluster the seismically slipping fault segments (i.e., sub-contacts) together to determine location and magnitude for events. We run our script every minute for the first 18 minutes of the models; the results are presented in Figure 43-45. The locations of the events are shown in Figure 43. Figure 44 presents a histogram of the number of events per magnitude range, and Figure 45 plots the magnitude of the events versus time for the 3 models. Model 1 predicts a total of 70 events with $M_w > 0$, 40 with $M_w > 1$, and 5 with $M_w > 1.5$, the largest a M_w 1.87, after 4 minutes of injection. Model 2 predicts a lower seismicity rate and maximum magnitude than model 1. Model 2 predicts a total of 42 events with $M_w > 0$, 20 with $M_w > 1$ and 4 with $M_w > 1.5$, the largest a M_w 1.67 after 16

minutes of injection. Model 3 predicts the fewest number of events; however, it also predicts the largest maximum magnitude event. A total of 36 events with $M_w > 0$, 19 with $M_w > 1$ and 2 with $M_w > 2$ are predicted by model 3. A $M_w 2.19$ event is predicted after 4 minutes of injection and a $M_w 2.15$ event is predicted after 7 minutes of injection. The first event predicted by model 3 was the $M_w 2.19$ event after 4 minutes of injections, while the $M_w 1.87$ event predicted after 4 minutes by model 1 (i.e., the largest event predicted by model 1) was preceded by 4 events with $M > 1$.

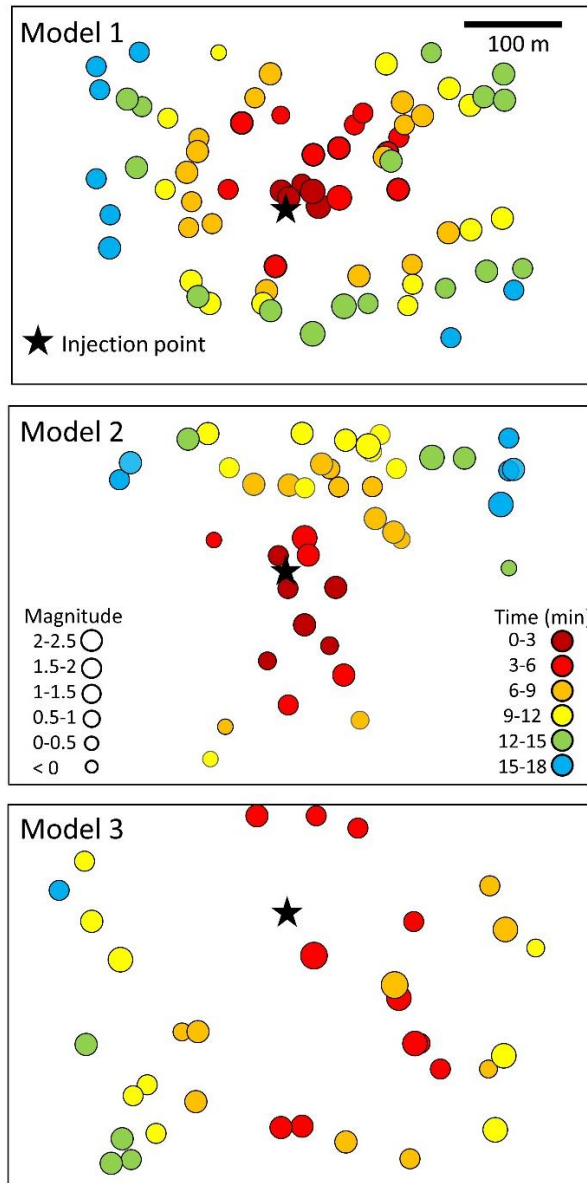


Figure 43. Location of seismic events on the fault (cross-sectional view) calculated for model 1 (top), model 2 (middle), and model 3 (bottom). Circle color indicates when the event occurred (since the start of injection) and circle size indicates the magnitude of the event. Black star marks the location of the injection on the center hydraulic fracture plane.

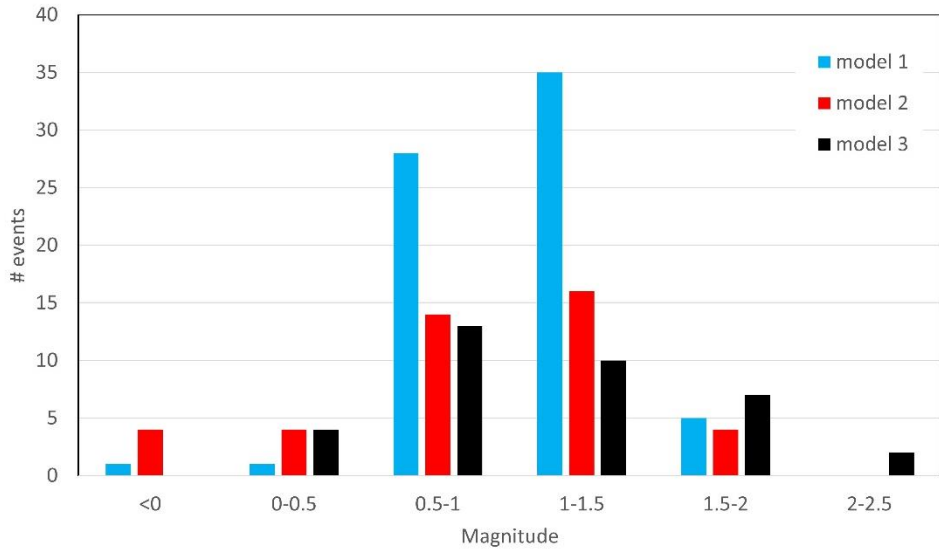


Figure 44. Histogram showing the number of events per magnitude range for the 3 models.

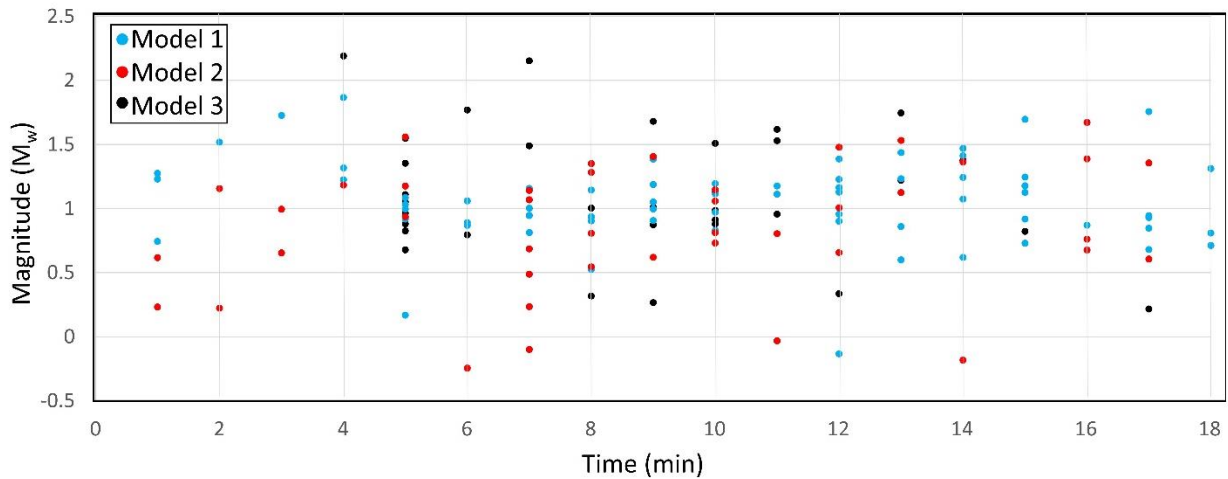


Figure 45. Plot of calculated moment magnitude versus time for the 3 models.

The results from our models simulated with the nonlinear softening-healing Coulomb joint model are similar to those with the Mohr-Coulomb joint model. However, fewer, higher magnitude events are predicted by the models with the nonlinear softening-healing Coulomb model. Model 1 predicts 5 events, all with $M_w > 1$, the largest, the last event recorded, with $M_w 2.32$, whereas model 3 also predicts 5 events, all with $M_w > 1$, but the largest is the first event recorded with $M_w 2.65$.

The results from our modelling suggest that the slip-weakening case, simulated by our model 1, predicts events which follow a pattern typical of a pore pressure diffusion model, with the largest events occurring later in time. Such a model may occur for critically-stressed faults for which slip-weakening

may occur despite the high pore pressures favoring slip-strengthening. We suggest this is similar to what was observed for the operation at pad 4, unintentionally monitored by our dense array deployment. In contrast, fewer events with larger magnitudes, earlier in time, are predicted for our model 3, which represents the cases when aseismic slip triggers seismic slip. We suggest such a model may occur on non-critically oriented faults where the aseismic slip outpaces pore pressure diffusion, and we propose this is the mechanism responsible for the M>4 events recorded in the Montney. Our model 2, which represents the slip-strengthening case, predicts the largest number of M<0.5 events and the lowest maximum magnitude events. We suggest such a model may occur on non-critically oriented faults where pore pressure diffusion outpaces the aseismic slip and we propose this is the mechanism responsible for the events observed for the operation on pad 2, unintentionally monitored by our dense array deployment.

Further modelling is needed to investigate this conceptual model, such as, clustering the seismicity in time as well as space, as well as testing different stress conditions. In particular, a reverse faulting stress regime should be tested as moment tensors for events in the Montney show a mixture of strike-slip and reverse or thrust faulting (Babaie Mahani et al., 2019). In addition, these results suggest more research is needed in understanding fault friction and how it evolves with slip and time during fluid injection.

Discussion and Conclusions

The primary objective of this project was to develop a low-cost alternative to local broadband arrays for monitoring hydraulic fracturing operations. We have demonstrated that with the time and funding for proper site investigation and station installation, an array such as we have designed can be used in combination with nearby regional broadband stations and an accurate velocity model to provide a monitoring alternative with comparable accuracy to local broadband arrays. In addition, we have shown that one of our accelerographs can replace a force-balance accelerometer (FBA) for the British Columbia Oil and Gas Commission's (BCOGC) required ground motion monitoring in the Montney. We further show that using a dense array of accelerometers is required to understand variations in ground motions. Additionally, we have shown that our array can detect hundreds of operationally-induced events for even small hydraulic fracturing operations. Data for these events are necessary for progressing our understanding of AIS and our ability to prevent and mitigate AIS. As operationally-induced events are critical for research into AIS and this data is not readily available without microseismic operations, which are not in real-time, or unrealistically dense broadband arrays, we have shown that using a geophone array with an automatic system, such as the one presented here, is a good option. The event detection using commercial geophones and automatic systems is not a new technology, it is an application of existing

methods, which should be more greatly exploited to obtain solutions for operationally-induced events (i.e., $M < 1$).

We have thoroughly tested our three-component (3C) accelerographs and our sensors have fulfilled the requirement of the BCOGC for the ground motion monitoring of 8 hydraulic fracturing operations in the Montney. During our sensor deployments, our accelerometers detected 72 events, with magnitudes up to 4.5 and hypocentral distances from 2.46 to 17.8 km. These events had site-corrected, peak-ground accelerations (PGA) ranging from 0.265 to 60.9 cm/s² (0.027 to 6.2 %g). In the past year (2019-2020), our 15 stations were upgraded to include commercial, 5 Hz, high precision, 3C geophones in order to obtain event information for operationally-induced events. Nine of our paired stations were installed to monitor a small hydraulic fracturing operation in the Montney in the Fall of 2020. Due to the current COVID-19 pandemic coupled with the industry slow-down, this was the first opportunity to test our paired array and as a result of short notice from the operator and ground conditions due to unseasonal weather, the installation was less than ideal. During the deployment, there were two additional hydraulic fracturing operations within the monitoring area, one overlapping in time with the main operation (pad 2) we were monitoring and the other following the second operation (pad 3). A fourth hydraulic fracturing operation (pad 4) was also completed at the same time, 26 km southeast from the pad we were monitoring. Nine events were recorded by the accelerometers during the deployment, seven of which occurred after the main operation. The largest of the events, a $M \sim 3$ located 20-30 km from our stations, was recorded by 6 of the 7 accelerometers functioning at the time. While the ground motions decrease with hypocentral distance for this $M \sim 3$ event, the ground motions for three other events that were recorded by more than 3 stations show distinct asymmetry, which cannot be explained by station effects, noise, or attenuation. We propose the observed asymmetry may result from rupture directivity resulting from the source mechanisms.

Three-hundred and thirty-five additional operationally-induced events ($M < 0.8$) were detected by our geophones during a 14-day period encompassing the main hydraulic fracturing operation. Automatic solutions for the events were obtained using the software SeisComP3. A second SeisComP3 pipeline was set up using the regional broadband stations with real-time data available through IRIS in combination with our geophone data, which detected 26 anomalous induced events ($M > 0.8$). A further 37 anomalous induced events were located using SeisComP3 in offline mode for an additional 5-day period. The majority of the anomalous induced events locate to the south of pads 2 and 3 and appear to follow a linear southeast-northwest trend, indicative of a fault. Our system also detected 156 events with $M_{\max} 3.2$ induced by the operation on pad 4. These events appear to trend along a feature critically-oriented with

respect to the regional stress field, while the fewer events with lower maximum magnitude detected near pads 2 and 3 are located along a feature that is non-critically oriented.

Early models conceptualized induced seismicity as resulting from seismic slip on faults directly induced by the diffusion of increased pore pressures from fluid injection; however, the largest events recorded in the Montney do not follow the pattern predicted by the pore pressure diffusion model. The largest event we recorded, the only M>4 induced by hydraulic fracturing to date in the KSMMA was not preceded by any yellow-light events (M>2) and occurred early in the sequence of events. The largest event induced by hydraulic fracturing recorded in the Montney was also not preceded by yellow-light events. Therefore, the most hazardous events induced in the Montney did not follow the anticipated pore pressure diffusion model and could not have been mitigated by traffic light protocols. Therefore, a better understanding of the processes controlling the magnitude and frequency of anomalous events induced by hydraulic fracturing operations is needed to develop better protocols for mitigation and prevention.

Through 3D hydro-geomechanical modelling, we have tested a newer conceptual model, where fluid injection induces aseismic slip on a fault, which then triggers seismic slip. The goal was to understand if such a process can explain why the two largest events induced by hydraulic fracturing in the Montney did not follow the anticipated pore pressure diffusion model, while many other operations do. By comparing models with different residual friction values for the fault, we suggest the mechanisms responsible for the observed variations in anomalous seismicity induced by hydraulic fracturing. A model with slip-weakening may account for seismicity observed to follow patterns typical of a pore pressure diffusion model, with events increasing in magnitude with injection time. Such a model may occur for critically-stressed faults for which slip-weakening may occur despite the high pore pressures favoring slip-strengthening. We suggest this is similar to what was observed for the operation at pad 4, which was unintentionally monitored by our dense array deployment. In comparison, the slip-strengthening case predicts fewer, lower magnitude events with the maximum magnitude event occurring earlier in time. We suggest such a model may occur on non-critically oriented faults where pore pressure diffusion outpaces the aseismic slip and we propose this is the mechanism responsible for the events observed for the operation on pads 2 and 3, unintentionally monitored by our dense array deployment. The most hazardous events are predicted by a model with slip strengthening near the fluid injection and slip-weakening on the outer fault. Such a model predicts the highest magnitude events, early in time, without precursor events with M>2. We suggest this mechanism is responsible for the M>4 events induced by hydraulic fracturing observed in the Montney.

Acknowledgments

We thank Geoscience BC for their support and funding for this study. We also thank K. Johansen and C. Ventura for their help with the design and construction of our sensors. Additionally, we thank J. Hazzard and the Itasca Consulting Group Inc. for their technical support.

References

- Babaie Mahani, A. and Kao, H. (2017). Ground motion from M1.5 to 3.8 induced earthquakes at hypocentral distance <45 km in the Montney play of northeast British Columbia, Canada, Seismological Research Letters, doi: 10.1785/0220170119.
- Babaie Mahani, A., Kao, H., Atkinson, G.M, Assatourians, K., Addo, K., and Liu, Y. (2019). Ground-motion characteristics of the 30 November 2018 injection-induced earthquake sequence in northeast British Columbia, Canada, Seismological Research Letters, 90, 1457-1467/0220170119.
- Babaie Mahani, A., F. Esfahani, H. Kao, M. Gaucher, M. Hayes, R. Visser, and S. Venables (2019). A Systematic Study of Earthquake Source Mechanism and Regional Stress Field in the Southern Montney Unconventional Play of Northeast British Columbia, Canada, Seismol. Res. Lett. 91, 195–206, doi: 10.1785/0220190230.
- Babaie Mahani, A. and H. Kao (2020). Determination of Local Magnitude for Induced Earthquakes in the Western Canada Sedimentary Basin: An Update, RECORDER, 45.
- Bhattacharya, P, and Viesca, R. 2019. Fluid-injection aseismic fault slip outpaces pore-fluid migration, Science 364, 464–468 (2019).
- Cappa, F., Guglielmi, Y., Nussbaum, C., Birkholzer, J. 2018. On the Relationship Between Fault Permeability Increases, Induced Stress Perturbation, and the Growth of Aseismic Slip During Fluid Injection, Geophysical Research Letters, 45, <https://doi.org/10.1029/2018GL080233>
- Cappa, F., Scuderi, M.M. Collettini, C., Guglielmi, Y., and Avouac, J.-P. 2019. Stabilization of fault slip by fluid injection in the laboratory and in situ, Science Advances, 5, DOI: 10.1126/sciadv.aau4065.
- Eyre, T.S., Eaton, D.W., Garagash, D.I., Zecevic, M., Venier M., Weir, R., Lawton, D.C. 2019. The role of aseismic slip in hydraulic fracturing-induced seismicity, Science Advances, 5, DOI: 10.1126/sciadv.aav7172.
- Fox, A. and Watson, N. 2019. Induced Seismicity Study in the Kiskatinaw Seismic Monitoring and Mitigation Area, British Columbia, report for BCOGC.

- Guglielmi Y, Nussbaum C, Jeanne P, Rutqvist J, Cappa F, Birkholzer J. 2020. Complexity of Fault Rupture and Fluid Leakage in Shale: Insights From a Controlled Fault Activation Experiment. *Journal of Geophysical Research: Solid Earth*, 125, e2019JB017781. <https://doi.org/10.1029/2019JB017781>
- Hassani, B., and G. M. Atkinson (2016). Applicability of the site fundamental frequency as a VS30 proxy for central and eastern North America, *Bulletin of Seismological Society of America*. 106, 653–664.
- Interstate Oil and Gas Compact Commission IOGCC (2015). Potential Injection-Induced Seismicity Associated with Oil & Gas Development: A Primer on Technical and Regulatory Considerations Informing Risk Management and Mitigation.
iogcc.publishpath.com/Websites/iogcc/images/2015OKC/ISWG_Primer_Final-Web.pdf. Accessed 2015/11/26.
- Itasca Consulting Group, Inc. (2020) *3DEC — Three-Dimensional Distinct Element Code, Ver. 7.0*. Minneapolis: Itasca.
- Li, Z., Z. Peng, D. Hollis, L. Zhu, and J. McClellan (2018). High-resolution seismic event detection using local similarity for Large-N arrays, *Sci. Rep.*, 8, 1646. doi:10.1038/s41598-018-19728-w
- Rosenberger, A. (2010). Internet Accelerograph: Realtime signal processing in V2.0., Geological Survey of Canada.
- Scientific Hydraulic Fracturing Review Panel, 2019. Scientific Review of Hydraulic Fracturing in British Columbia, Ministry of Energy, Mines and Petroleum Resources, p. 236.
- Scuderi, M.M. and Colletini, C. (2018). Fluid injection and the mechanics of frictional stability of shale-bearing faults. *Journal of Geophysical Research: Solid Earth*, 123, 8364-8384.
- Seyhan, E., and J. P. Stewart (2014). Semi-empirical nonlinear site amplification from NGA-West2 data and simulations, *Earthq. Spectra* 30, 1241–1256.
- Visser, R., Kao, H., Smith, B., Goerzen, C., Kontou, B., Dokht, R.M.H., Hutchinson, J., Tan, F., Babaie Mahani, A. 2020. A comprehensive earthquake catalogue for the Fort St. John-Dawson Creek region, British Columbia, 2017-2018, Geological Survey of Canada, Open File 8718, doi:10.4095/326015
- Wynants-Morel, N., Cappa, F., De Barros, L., and Ampuero, J.-P. 2020. Stress perturbation from aseismic slip drives the seismic front during fluid injection in a permeable fault. *Journal of Geophysical Research, Solid Earth*, 125 doi:101029/2019JB019179
- Yenier, E., Laporte, M., and Baturan, D, 2017. Induced seismicity monitoring: Broadband seismometers and geophone comparison. https://www.nanometrics.ca/sites/default/files/2017-11/ism_bb_seismometer_geophone_comparison.pdf

Yin, Z., Huang, H., Zhang, F., Zhang, L., and Maxwell, S. 2020. Three-dimensional distinct element modeling of fault reactivation and induced seismicity due to hydraulic fracturing injection and backflow, Journal of Rock Mechanics and Geotechnical Engineering, 12, doi:10.1016/j.jrmge.2019.12.009.

Zhang, F., Yin, Z., Chen, Z., Maxwell, S. Zhang, L., and Wu, Y. 2020. Fault reactivation and induced seismicity during multi-stage hydraulic fracturing: microseismic analysis and geomechanical modelling, SPE Jounral doi:10.2188/199883-PA.

Appendix 1

● **MAIN SPECIFICATION:**

GEOPHONE ELEMENT (PS-4.5B): (20 °C)

Frequency:

Natural frequency	4.5Hz
Tolerance	+/- 10%

Distortion:

Distortion with 0.7 in/s p.p. coil to Case velocity	≤0.3%
Distortion measurement frequency	12Hz

Damping

Typical open circuit damping	0.60
Tolerance with calibration shunt	+/- 10%

Coil Resistance

Standard	375 Ω
Tolerance	+/- 5%

Sensitivity

Sensitivity	28.8 V/m/s
Tolerance	+/- 7%
Moving mass	11.3 g
Maximum coil excursion p.p.	4 mm

Physical Characteristics

Diameter	25.4 mm
Height	36 mm
Weight	80g
Operating temperature range	-40°C to 70°C
Warranty period	1 year

Appendix 2

Operation	Event	Site ID	PGA _h (cm/s ²)	Distance (km)	M _w LBA	M _L NRCan	M _L Visser ¹
1-2	1	13	0.540	4.90	2.23		2
		04	0.960	4.50			
	2	13	0.310	17.50	2.88	3	2.8
		04	2.22	9.10			
2	1	13	0.360	5.60	1.57		1.4
	2	13	0.330	6.40	1.72		1.6
	3	13	0.460	5.10	1.88		1.9
	4	13	0.300	4.60	1.74		1.6
	5	13	0.520	5.90	1.54		
	6	13	0.310	4.60	1.62		1.5
3	1	03	0.680	1.20	1.74		
	2	03	0.550	2.20	1.77		1.6
	3	03	0.270	5.00	1.64		1.3
	4	03	0.480	5.90	1.8		
5	1	16	3.60	5.90	2.02		2
		13	1.14	6.92			
	2	16	0.589	3.60	1.57		1.5
	3	13	0.529	5.35	1.62		1.3
6 ³	1	16	1.17	4.64	1.70		1.6
	2	16	0.505	5.59	1.85		1.7
	3	16	60.9	5.41	3.95	4.5 ²	4.5 ²
	4	16	0.684	5.01	1.71		2
	5	16	0.476	4.64	1.61		1.7
	6	16	15.0	5.21	2.95	3.4	3.3
	7	16	19.7	5.16	3.42	4.0	3.9
	8	16	0.62	5.87	2.17		2.1
	9	16	0.31		<1.5		
	10	16	0.58	5.80	1.75		1.8
	11	16	1.15	4.95	1.96		1.8
	12	16	0.65	4.45	1.61		1.6
	13	16	2.28	5.76	2.33	2.7	2.4
		13	1.65	6.19			
	14	16	0.452	6.24	1.78		1.7
	15	16	2.03	4.12	1.78		1.8
		13	0.547	5.14			
	16	16	0.210	6.95	1.75		1.4
	17	16	4.95	2.46	2.18		2.1
	18	16	2.54	6.33	2.7		

			13	1.52	6.67
6-7	1	16	0.287	17.8	2
	2	16	0.400	12.5	1.8
		13	0.277	13.4	
	3	16	0.376	8.74	2.3
	4	16	0.293	4.52	2.1
	5	16	0.585	16.0	2.1
		13	0.376	17.0	
7	1	16	0.356	8.12	2.38
		13	0.294	7.14	
	2	16	0.360	3.65	1.63
	3	16	7.26		<1.5
		13	1.43		
	4	16	2.21	3.01	1.61
		13	1.42	3.55	
	5	16	0.380		<1.5
		13	0.239		
	6	16	3.34	7.08	2.4
		13	1.00	8.12	
	7	16	0.296		<1.5
		13	0.226		
8	16	0.477		<1.5	
	13	0.258			
9	16	1.44		<1.5	
	13	0.402			
10	16	0.351		<1.5	
	13	0.233			
11	16	0.326		<1.5	
	13	0.237			
12	16	0.344		<1.5	
	13	0.253			
13	16	0.339		<1.5	
	13	0.213			
14	16	0.785		<1.5	
	13	0.258			
15	16	0.759	4.33	1.63	
	13	0.339	5.30		
16	16	2.43	4.72	1.99	
	13	1.06	5.68		
17	16	1.80	4.37	2.26	2.1
	13	1.85	5.36		
18	16	0.448	5.51	1.90	

	13	0.361	6.56	
19	16	0.335		<1.5
	13	0.345		
20	16	0.311	5.60	1.67
	13	0.244	6.64	
21	16	0.418	5.34	1.63
	13	0.247	6.38	
22	16	0.379		<1.5
	13	0.264		
23	16	1.25	4.33	1.93
	13	0.746	5.00	
24	16	0.347	5.40	1.62
25	16	0.319		<1.5
26	16	0.325		<1.5
	13	0.248		
8	A	18	0.625	1.71
	B	16	0.951	4.88
		18	0.523	6.26
		20	0.567	6.08
		22	0.540	9.31
	C	16	0.629	8.50
		18	1.12	10.8
		20	1.96	7.45
		21	0.671	13.1
		22	2.63	7.45
		25	0.564	12.6
	D	22	0.593	2.5
	E	16	0.662	4.23
		18	1.57	2.58
		20	0.568	7.71
		25	0.467	6.92
	F	16	0.535	24.3
		18	0.374	26.7
		20	0.641	22.1
		21	0.377	28.3
		22	0.896	19.3
		25	0.542	28.3
	G	16	0.480	1.65
		18	0.639	
	H	16	0.512	<1.5
		18	0.560	
		25	1.41	

I	16	0.686	1.60
	18	0.512	

LBA= Local broadband array

¹ Visser et al. (2020)

² M_w

³ Station 13 had technical issues for part of this operation

Appendix 3

Event ID	Distance from pad1 (km)	Bearing from pad1 (°)	M_L
1	25.2	236	
2	8.7	221	
3	9.0	203	0.35
4	12.1	253	
5	7.8	217	
6	11.1	232	
7	0.3	178	
8	6.1	229	
9	9.9	214	
10	9.2	237	
11	5.4	235	
12	14.7	256	
13	7.0	235	
14	8.1	222	
15	5.4	200	
16	4.8	202	
17	15.0	213	
18	15.6	235	
19	20.1	230	
20	2.8	169	
21	11.3	236	
22	14.7	250	
23	11.2	218	
24	1.4	185	
25	1.0	183	
26	16.3	267	
27	14.6	248	
28	15.0	237	
29	0.3	177	
30	17.6	247	
31	5.6	217	
32	3.2	196	
33	13.8	224	
34	7.2	213	
35	6.0	160	0.57
36	7.4	297	
37	12.5	239	
38	16.3	259	
39	8.7	305	

40	12.5	247
41	7.4	264
42	6.8	207
43	16.9	228
44	11.2	223
45	11.2	229
46	1.4	187
47	4.1	152
48	10.4	251
49	14.0	272
50	4.8	237
51	15.5	129
52	8.7	314
53	4.1	164
54	8.7	238
55	16.1	34 1.13
56	5.2	216
57	6.8	208
58	4.4	301
59	4.8	220
60	4.8	308
61	14.4	216
62	0.3	162
63	15.0	250
64	19.4	251
65	0.5	182
66	3.6	214
67	6.7	196 0.49
68	11.2	208
69	14.2	225
70	1.4	204
71	4.8	194
72	6.1	139
73	11.2	223
74	8.7	231
75	9.9	219
76	3.3	208
77	3.6	205
78	18.9	225
79	15.0	243
80	8.7	216
81	17.6	235
82	5.1	194

83	3.9	168
84	16.1	218
85	8.7	215
86	20.1	239
87	16.2	129 1.42
88	16.9	128 1.07
89	1.0	347
90	8.3	212
91	11.1	286
92	19.1	244
93	0.5	178
94	5.3	329
95	18.9	254
96	12.5	227
97	16.3	245
98	17.4	255
99	9.9	278
100	13.7	248
101	14.2	221
102	17.7	243
103	3.5	275
104	12.6	219
105	1.8	168
106	19.4	257
107	9.1	229
108	16.3	233
109	12.6	304
110	4.8	308
111	6.2	208
112	22.7	290
113	4.6	55
114	5.9	75
115	1.1	168
116	5.9	75 1.17
117	14.6	225
118	13.8	241
119	15.4	262
120	13.8	285
121	12.4	315
122	11.2	236
123	14.3	220
124	10.3	305
125	14.3	109

126	4.5	226	
127	18.9	216	
128	2.4	264	
129	6.0	248	
130	10.1	218	
131	24.5	253	
132	8.7	207	
133	20.5	229	
134	1.4	172	
135	13.8	249	
136	11.2	277	
137	1.0	191	
138	9.9	242	
139	9.9	265	
140	7.4	211	
141	6.1	-36	
142	18.9	242	
143	13.3	255	
144	10.6	226	
145	7.4	224	
146	9.0	243	
147	18.8	268	
148	15.0	231	
149	2.3	186	
150	15.5	242	
151	0.7	174	
152	16.0	129	
153	13.8	234	
154	6.1	284	
155	2.8	170	
156	1.5	176	
157	7.3	202	
158	1.0	182	
159	13.7	219	
160	30.3	269	
A/161	4.7	115	1.51
162	6.1	193	
163	20.1	287	
164	15.5	127	1.37
165	6.6	146	
166	15.0	258	
167	2.8	10	
168	15.4	127	1.44

169	8.7	117	
170	15.2	255	
171	0.3	181	0.67
172	11.2	244	
173	4.1	169	
174	3.4	210	
175	10.4	229	
176	2.9	188	
177	19.4	237	
178	9.7	218	
179	8.7	211	
180	0.2	182	
181	15.3	128	1.66
182	12.1	238	
183	14.4	227	
184	20.1	221	
185	15.3	127	1.67
186	8.5	222	
187	12.4	225	
188	22.1	265	
189	1.0	175	
190	4.6	225	
191	6.1	219	
192	3.4	221	
193	4.1	26	
194	11.7	222	
195	2.5	158	
196	16.3	240	
197	4.8	198	
198	7.0	293	
199	1.6	143	
200	9.3	213	
201	4.4	246	
202	10.0	224	
203	5.0	210	
204	3.2	324	
205	13.2	237	
206	3.3	135	
207	2.7	201	
208	13.0	244	
209	9.5	250	
210	19.1	242	
211	10.4	239	

212	14.1	244	
213	1.9	192	
214	2.0	322	
215	14.9	130	
216	8.9	239	
217	18.6	261	
218	0.1	182	
219	3.2	168	
220	18.6	266	
221	7.2	223	
222	9.2	231	
223	14.3	317	
224	1.0	173	
225	4.1	220	
226	9.1	243	
227	3.4	204	
228	12.0	237	
229	9.2	199	
230	2.6	241	
231	1.8	191	
232	11.7	262	
233	4.0	209	
234	1.2	294	
235	4.3	249	
236	14.8	127	1.09
237	14.2	129	1.57
238	3.2	140	
239	16.5	249	
240	14.8	130	1.49
241	3.6	200	
242	2.6	141	
243	20.7	267	
244	8.8	220	
245	26.9	247	
246	4.7	202	
247	5.1	149	
248	3.6	192	
249	5.9	213	
250	14.7	128	1.45
251	12.6	237	
252	6.4	448	
253	1.0	223	
254	6.8	214	

255	16.3	219
256	5.1	266
257	5.1	210
258	5.9	213
259	10.9	229
260	0.7	174
261	4.6	190
262	16.3	221
263	17.9	230
264	14.3	228
265	2.8	122
266	14.1	129 1.45
267	1.1	176
268	2.5	195
269	3.8	199
270	4.7	210
271	11.9	227
272	10.0	228
273	1.2	175
274	7.9	112 0.75
275	1.1	173
276	14.0	129 1.74
277	4.6	279
278	1.2	174
279	10.4	242
280	0.6	184
281	1.1	187
282	3.4	133
283	4.7	290
284	3.9	157
285	5.7	206
286	3.3	164
287	17.6	301
288	11.6	252
289	4.5	28
290	9.3	297
291	3.7	199
292	0.0	181
293	1.2	193
294	9.5	221
295	16.0	283
296	13.2	241
297	7.8	220

298	13.9	128	1.41
299	10.1	234	
300	3.0	195	
301	0.8	183	
302	3.9	221	
303	6.3	199	
304	6.0	207	
305	10.5	252	
306	17.1	229	
307	7.5	214	
308	6.9	223	
309	3.3	144	
310	0.8	172	
311	9.7	215	
312	13.1	227	
313	13.9	130	1.45
314	11.9	126	0.92
315	5.0	200	
316	3.8	216	
317	8.0	217	
318	10.1	235	
319	4.5	216	
320	4.2	324	
321	4.2	206	
322	2.7	164	
323	10.8	221	
324	9.9	209	
325	3.1	213	
326	8.4	225	
327	5.2	196	
328	7.1	216	
329	10.8	233	
330	2.8	247	
331	4.4	155	
332	9.9	121	
333	9.9	121	
334	7.4	215	
335	9.6	268	
336	5.1	241	
337	9.3	208	
338	8.2	213	
339	1.0	185	
340	8.5	256	

341	14.1	127	1
342	1.7	192	
343	0.7	184	
344	14.0	127	1.21
345	2.5	165	
346	12.0	227	
347	14.0	129	1.42
348	14.6	128	0.68
349	7.1	217	
350	11.5	247	
351	7.9	218	
352	15.8	239	
B/353	9.1	117	1.96
354	12.1	127	
355	2.6	188	
356	4.6	167	
357	3.0	202	
358	3.5	71	
359	14.1	128	1.44
360	2.5	161	
361	1.7	189	
362	15.1	129	0.76
363	7.6	277	
C/364	14.9	131	2.29
365	13.8	127	1.2
366	14.3	128	1.03
367	14.0	127	0.83
368	14.2	127	0.89
369	14.0	128	0.7
D/370	46.5	124	2.49
371	13.4	130	1.39
372	13.6	127	1.32
E/373	4.0	65	1.64
374	12.7	128	1.94
375	13.7	128	1.37
376	14.0	130	0.73
377	13.7	128	0.78
378	48.0	125	2.4
379	13.5	129	1.31
380	13.0	128	1.38
381	13.3	128	1.41
382	13.9	128	1.27
383	12.8	128	1.48

384	13.6	129	1.19
385	13.8	129	0.65
386	12.8	128	0.99
387	6.8	260	1.08
388	5.6	260	1.07
389	13.0	127	1.13
390	12.8	128	0.92
391	12.3	128	1.35
392	13.5	129	0.55
393	12.5	126	1.68
394	44.5	130	2.2
395	13.6	128	0.94
F/396	44.7	125	3.17
397	3.8	58	1.65
398	12.8	128	1.13
399	13.4	126	1.57
400	13.1	128	0.89
401	12.4	134	0.69
G/402	6.8	254	1.27
H/403	5.2	107	1.5